

# LATENT AUTO-ENCODER ENSEMBLE KALMAN FILTER FOR NONLINEAR DATA ASSIMILATION\*

XIN T. TONG <sup>†</sup>, YANYAN WANG<sup>‡</sup>, AND LIANG YAN<sup>§</sup>

**Abstract.** The ensemble Kalman filter (EnKF) is widely used for data assimilation in high-dimensional systems, but its performance often deteriorates for strongly nonlinear dynamics due to the structural mismatch between the Kalman update and the underlying system behavior. In this work, we propose a latent autoencoder ensemble Kalman filter (LAE-EnKF) that addresses this limitation by reformulating the assimilation problem in a learned latent space with linear and stable dynamics. The proposed method learns a nonlinear encoder–decoder together with a stable linear latent evolution operator and a consistent latent observation mapping, yielding a closed linear state-space model in the latent coordinates. This construction restores compatibility with the Kalman filtering framework and allows both forecast and analysis steps to be carried out entirely in the latent space. Compared with existing autoencoder-based and latent assimilation approaches that rely on unconstrained nonlinear latent dynamics, the proposed formulation emphasizes structural consistency, stability, and interpretability. We provide a theoretical analysis of learning linear dynamics on low-dimensional manifolds and establish generalization error bounds for the proposed latent model. Numerical experiments on representative nonlinear and chaotic systems demonstrate that the LAE-EnKF yields more accurate and stable assimilation than the standard EnKF and related latent-space methods, while maintaining comparable computational cost and data-driven.

**Key words.** Data Assimilation; Ensemble Kalman Filter; Latent Space.

**MSC codes.** 68T07,37M05,65P99, 65C20

**1. Introduction.** Data assimilation (DA) optimally integrates dynamical model predictions with noisy and incomplete observations to estimate the evolving state of complex systems. In practice, it combines heterogeneous data sources, such as in-situ measurements, satellite retrievals, and radar observations, with either physics-based or data-driven models of the underlying dynamics. By providing a systematic framework for uncertainty-aware state estimation, DA serves as a foundational methodology across numerous scientific and engineering fields, including numerical weather prediction, climate science, geophysics, hydrology, and economics [19].

From a probabilistic perspective, DA can be formulated as a Bayesian filtering problem [30], where the goal is to sequentially infer the posterior distribution of the system state conditioned on all available observations. Among approximate Bayesian filtering methods, the ensemble Kalman filter (EnKF) [17] has become one of the most widely adopted techniques due to its favorable computational scaling, derivative-free implementation, and ensemble-based representation of uncertainty. For linear systems with Gaussian noise, the EnKF provides a Monte Carlo approximation of the classical Kalman filter and converges to the exact Bayesian solution as the ensemble size increases. However, in realistic applications involving strongly nonlinear dynamics, partial observations, and non-Gaussian error statistics, the EnKF often becomes suboptimal and may even suffer from filter divergence [20]. Importantly, this degradation is not intrinsic to the Kalman update itself, but rather stems from a

---

\*Submitted to the editors DATE.

**Funding:** This work was supported by the NSF of China (Nos. 92370126, 12171085) and the Jiangsu Provincial Scientific Research Center of Applied Mathematics (grant BK20233002).

<sup>†</sup>Department of Mathematics, National University of Singapore, 119076, Singapore (xin.t.tong@nus.edu.sg)

<sup>‡</sup>School of Mathematics, Southeast University, Nanjing 210096, China (yanyanwang@seu.edu.cn)

<sup>§</sup>School of Mathematics, Southeast University, Nanjing 210096, China (yanliang@seu.edu.cn).

structural mismatch between the linear–Gaussian assumptions underlying the EnKF analysis step and the true nonlinear dynamics and observation processes. As a result, the posterior ensemble is effectively constrained to an affine subspace determined by local linearizations of the model and observation operator [30, 27], leading to biased estimates and loss of stability.

Extensive research has aimed to enhance the robustness of EnKF-type methods in nonlinear and non-Gaussian settings. Sigma-point filters, including the unscented and cubature Kalman filters, propagate carefully chosen samples through nonlinear models to improve moment approximations [18, 3]. Particle filters offer greater flexibility by representing the posterior with weighted ensembles [30], but they typically suffer from severe weight degeneracy in high-dimensional systems. Alternative approaches reinterpret the Bayesian update as a deterministic transport or flow of probability measures [31], while hybrid variational–ensemble methods incorporate gradient information to better handle nonlinear observation operators [9]. Despite these advances, achieving accurate, stable, and scalable filtering for strongly nonlinear, high-dimensional systems remains a fundamental challenge.

Recently, deep learning has emerged as a powerful tool for addressing nonlinear DA problems [4, 6, 10]. Neural networks have been used to learn surrogate dynamical models, approximate observation operators, and correct model error directly from data [37, 36, 14, 39]. While some approaches iteratively retrain networks during the assimilation cycle [7], such strategies are often impractical for real-time sequential filtering and may lack stability and interpretability. These limitations have motivated the development of *latent data assimilation* methods, which seek to reduce dimensionality and nonlinearity by performing DA in a learned low-dimensional latent space. One class of methods constructs surrogate dynamics in latent coordinates and incorporates observational corrections during time integration [24, 29]. A complementary class embeds both system states and observations into a latent space and performs filtering updates directly in latent variables [1, 2, 13]. However, in the presence of heterogeneous or strongly nonlinear observations, separate encoders are often required for states and observations, leading to mismatched latent representations and inconsistencies between forecast and analysis steps.

To address these issues, Chen et al. [15] proposed the multi-domain encoder–decoder latent assimilation (MEDLA) framework, which maps heterogeneous observations into a unified latent space using multiple encoders and decoders. While MEDLA improves flexibility under diverse observation settings, its latent dynamics are governed by unconstrained nonlinear neural operators, which can limit interpretability and long-term stability. In parallel, Koopman operator theory offers a complementary perspective by representing nonlinear dynamical systems through linear evolution in a suitably lifted feature space [8, 26]. Koopman autoencoders operationalize this idea by learning encoder–decoder pairs such that latent variables evolve under a learned linear operator [5, 28]. Crucially, linear latent dynamics provide improved interpretability, numerical stability, and structural compatibility with Kalman filtering.

Motivated by these observations, we propose in this paper the *latent autoencoder ensemble Kalman filter* (LAE-EnKF), which reformulates the DA problem through a structure-preserving latent dynamical representation. The proposed framework learns a nonlinear encoder–decoder pair that maps high-dimensional physical states onto a compact latent manifold, while explicitly enforcing stable linear latent dynamics. In contrast to generic autoencoder-based DA methods, all forecast and analysis operations are carried out directly in the learned latent coordinates, where the Kalman update is structurally justified. The approach is fully data-driven and applicable in settings

where the governing equations are partially known or unavailable. To accommodate heterogeneous and partially observed measurement settings, we further introduce an observation encoder that embeds observations into the same latent coordinate system as the state variables. This design yields a unified latent state-space model in which both the system dynamics and the observation process are linear in the latent variables, eliminating inconsistencies arising from mismatched latent representations. Owing to this structure, the intrinsic latent dimension required for accurate assimilation is often significantly smaller than the ambient physical dimension, leading to improved robustness and computational efficiency.

On the theoretical side, we analyze the proposed framework under a smooth manifold assumption and establish generalization error bounds for learning stable linear latent dynamics. Extensive numerical experiments on representative nonlinear and chaotic systems show that the proposed LAE-EnKF consistently improves assimilation accuracy, stability, and robustness compared with standard EnKF and existing autoencoder-assisted approaches, while maintaining favorable computational efficiency.

The remainder of this paper is organized as follows. Section 2 formulates the data assimilation problem and reviews the EnKF. Section 3 introduces the LAE-EnKF framework, including the latent representation, observation embedding, and filtering algorithm. Section 4 presents the theoretical analysis. Section 5 reports numerical results on several nonlinear and chaotic systems. Finally, Section 6 concludes the paper and discusses future research directions.

## 2. Data Assimilation.

**2.1. Problem formulation.** We consider a discrete-time dynamical system of the form

$$(2.1) \quad \mathbf{x}_k = \mathbf{F}(\mathbf{x}_{k-1}) + \mathbf{w}_k, \quad \mathbf{w}_k \sim \mathcal{N}(\mathbf{0}, \mathbf{Q}_k),$$

where  $\mathbf{x}_k \in \mathbb{R}^D$  denotes the system state at time  $t_k$ ,  $\mathbf{F}$  is a generally nonlinear evolution operator, and  $\mathbf{w}_k$  represents model error.

In many practical applications, such as numerical weather prediction and ocean circulation modeling, the full state  $\mathbf{x}_k$  is not directly observable [30]. Instead, at each time  $t_k$ , only partial and noisy observations are available:

$$(2.2) \quad \mathbf{y}_k = \mathcal{H}(\mathbf{x}_k) + \boldsymbol{\eta}_k, \quad \boldsymbol{\eta}_k \sim \mathcal{N}(\mathbf{0}, \boldsymbol{\Gamma}_k),$$

where  $\mathcal{H}$  is the observation operator and  $\boldsymbol{\eta}_k$  denotes observation noise.

Given observations  $Y_k = (\mathbf{y}_1, \dots, \mathbf{y}_k)$ , the objective of data assimilation is to approximate the filtering distribution  $p(\mathbf{x}_k | Y_k)$ . For nonlinear and high-dimensional systems, evaluating this posterior exactly is intractable [30], motivating the development of approximate Bayesian filtering methods.

**2.2. Ensemble Kalman filter.** The ensemble Kalman filter (EnKF) [17] is one of the most widely used approximate Bayesian filtering methods for large-scale systems. It represents uncertainty using a finite ensemble and propagates empirical means and covariances without requiring explicit derivatives of the dynamical model. Owing to its computational efficiency and scalability, the EnKF has become a standard tool in high-dimensional data assimilation.

At each assimilation cycle, the EnKF alternates between a forecast step and an analysis step. We summarize the standard formulation below to highlight the structural assumptions underlying the method, which are central to the developments in this paper.

*Initialization.* Given a prior mean  $\mathbf{m}_0$  and covariance  $\mathbf{P}_0$ , an initial ensemble

$$\widehat{\mathbf{x}}_0^{(1)}, \dots, \widehat{\mathbf{x}}_0^{(N_e)}$$

is drawn from the prior distribution. The forecast and analysis steps are then applied sequentially for  $k = 1, \dots, K$ .

*Forecast step.* Each ensemble member is propagated forward according to the nonlinear dynamical model (2.1):

$$\widehat{\mathbf{x}}_{k|k-1}^{(j)} = \mathbf{F}\left(\widehat{\mathbf{x}}_{k-1}^{(j)}\right) + \mathbf{w}_k^{(j)}, \quad j = 1, \dots, N_e,$$

where  $\widehat{\mathbf{x}}_{k|k-1}^{(j)}$  denotes the forecast of the  $j$ -th ensemble member at time  $t_k$  conditioned on observations up to  $t_{k-1}$ . The corresponding predicted observations are

$$\widehat{\mathbf{y}}_k^{(j)} = \mathcal{H}\left(\widehat{\mathbf{x}}_{k|k-1}^{(j)}\right).$$

The sample means are computed as

$$\bar{\mathbf{x}}_{k|k-1} = \frac{1}{N_e} \sum_{j=1}^{N_e} \widehat{\mathbf{x}}_{k|k-1}^{(j)}, \quad \bar{\mathbf{y}}_k = \frac{1}{N_e} \sum_{j=1}^{N_e} \widehat{\mathbf{y}}_k^{(j)}.$$

The sample cross-covariance and observation covariance are given by

$$\begin{aligned} \widehat{\mathbf{P}}_{xy} &= \frac{1}{N_e - 1} \sum_{j=1}^{N_e} (\widehat{\mathbf{x}}_{k|k-1}^{(j)} - \bar{\mathbf{x}}_{k|k-1})(\widehat{\mathbf{y}}_k^{(j)} - \bar{\mathbf{y}}_k)^\top, \\ \widehat{\mathbf{P}}_{yy} &= \frac{1}{N_e - 1} \sum_{j=1}^{N_e} (\widehat{\mathbf{y}}_k^{(j)} - \bar{\mathbf{y}}_k)(\widehat{\mathbf{y}}_k^{(j)} - \bar{\mathbf{y}}_k)^\top. \end{aligned}$$

*Analysis step.* The Kalman gain is approximated by

$$\widehat{\mathbf{K}}_k = \widehat{\mathbf{P}}_{xy}(\widehat{\mathbf{P}}_{yy} + \mathbf{\Gamma}_k)^{-1},$$

and the analysis ensemble is updated using the perturbed-observation formulation:

$$\widehat{\mathbf{x}}_k^{(j)} = \widehat{\mathbf{x}}_{k|k-1}^{(j)} + \widehat{\mathbf{K}}_k(\mathbf{y}_k + \boldsymbol{\eta}_k^{(j)} - \widehat{\mathbf{y}}_k^{(j)}), \quad \boldsymbol{\eta}_k^{(j)} \sim \mathcal{N}(\mathbf{0}, \mathbf{\Gamma}_k).$$

The EnKF thus provides an efficient and scalable approximation to Bayesian filtering, particularly for high-dimensional systems. For linear dynamics and Gaussian noise, it converges to the classical Kalman filter as the ensemble size increases. In nonlinear settings, however, the analysis step enforces an *affine* update based on sample covariances, implicitly assuming a locally linear and Gaussian posterior structure. As a result, the updated ensemble is restricted to the affine subspace spanned by the forecast ensemble, regardless of the true posterior geometry. This structural mismatch between the Kalman update and the nonlinear state space can lead to biased estimates, loss of ensemble diversity, and filter instability or divergence [30, 34]. These limitations motivate a representation-based reformulation of data assimilation, in which the system dynamics and observation process are embedded into a space where linear-Gaussian assumptions are more appropriate. In the next section, we introduce a latent-space framework that achieves this goal and enables ensemble Kalman filtering to be applied in a structurally consistent manner.

**3. Latent-Space Ensemble Kalman Filter.** As discussed in Section 2, the main limitation of the ensemble Kalman filter in nonlinear settings is not the Kalman update itself, but the mismatch between its linear–Gaussian structure and the nonlinear geometry of the physical state space. Rather than modifying the Kalman update, we adopt a representation-driven perspective and seek a transformation of the state and observation variables under which the assumptions of Kalman filtering are approximately satisfied.

Specifically, we reformulate data assimilation in a learned latent space where (i) the system dynamics evolve approximately linearly under a stable operator, and (ii) observations admit a consistent linear representation. This latent formulation restores structural compatibility with ensemble Kalman filtering, allowing forecast and analysis steps to be carried out in a principled manner while retaining the computational efficiency of ensemble-based methods.

**3.1. Latent autoencoder assimilation.** Let  $\mathbf{x}_k \in \mathbb{R}^D$  denote the physical state at time  $t_k$ . We introduce a nonlinear encoder  $\mathcal{E} : \mathbb{R}^D \rightarrow \mathbb{R}^n$ , which maps the physical state to a low-dimensional latent variable

$$(3.1) \quad \mathbf{z}_k = \mathcal{E}(\mathbf{x}_k),$$

together with a decoder  $\mathcal{D} : \mathbb{R}^n \rightarrow \mathbb{R}^D$ , which reconstructs the physical state via

$$(3.2) \quad \hat{\mathbf{x}}_k = \mathcal{D}(\mathbf{z}_k).$$

The central modeling assumption is that, although the physical dynamics are nonlinear, their evolution can be approximated by a *linear and stable* operator in a suitably chosen latent representation. Accordingly, we impose the latent transition model

$$(3.3) \quad \mathbf{z}_k = \mathbf{A}\mathbf{z}_{k-1},$$

where  $\mathbf{A} \in \mathbb{R}^{n \times n}$  is a trainable matrix. This construction is closely related to Koopman-based representations [5, 28], in which nonlinear dynamics are lifted to linear evolution in a learned feature space. Crucially, the explicit linear structure of (3.3) is not merely a modeling convenience, but a deliberate design choice that enables structural compatibility with Kalman filtering.

To avoid inconsistencies between forecast and analysis steps, the observation process is embedded into the same latent coordinate system. Let  $\mathbf{y}_k \in \mathbb{R}^{D_y}$  denote the observation at time  $t_k$ . An observation encoder  $\mathcal{E}_{\text{obs}} : \mathbb{R}^{D_y} \rightarrow \mathbb{R}^m$  maps observations to latent variables

$$(3.4) \quad \tilde{\mathbf{y}}_k = \mathcal{E}_{\text{obs}}(\mathbf{y}_k),$$

which are related to the latent state through the linear model

$$(3.5) \quad \tilde{\mathbf{y}}_k = \mathbf{H}\mathbf{z}_k + \tilde{\boldsymbol{\eta}}_k, \quad \tilde{\boldsymbol{\eta}}_k \sim \mathcal{N}(\mathbf{0}, \tilde{\boldsymbol{\Gamma}}_k).$$

Here  $\mathbf{H} \in \mathbb{R}^{m \times n}$  is a prescribed or learned observation matrix. By embedding both states and observations into a common latent space, we obtain a closed linear state-space system in the latent variables. This construction eliminates the latent-space mismatch that arises when state evolution and observation mapping are learned independently, and provides a consistent foundation for Kalman-type updates.

**3.2. Network architecture and learning framework.** The latent autoencoder (LAE) framework consists of a state encoder  $\mathcal{E}$ , a decoder  $\mathcal{D}$ , a latent linear transition operator  $\mathbf{A}$ , and an observation encoder  $\mathcal{E}_{\text{obs}}$ , as illustrated in Fig. 1. The central objective is to learn a low-dimensional representation that is expressive enough to capture nonlinear system dynamics, while enforcing a structure that is compatible with linear–Gaussian filtering. In particular, the learned latent representation is designed so that the system evolution and observation process admit linear models, thereby restoring structural consistency with ensemble Kalman filtering.

To this end, we adopt a two-stage training strategy. The first stage focuses on learning a stable latent linear dynamical system from state trajectories. The second stage aligns observations with the learned latent state, ensuring consistency between forecast and analysis steps in the subsequent filtering procedure.

*Stage I: learning stable latent linear dynamics.* Given  $N_{\text{traj}}$  training trajectories  $\{\mathbf{x}_k^{(i)}\}$  of length  $K$ , the encoder  $\mathcal{E}$ , decoder  $\mathcal{D}$ , and latent transition matrix  $\mathbf{A}$  are trained jointly by minimizing

$$\begin{aligned} \mathcal{L}_{\text{lat}}(\mathcal{E}, \mathcal{D}, \mathbf{A}) = & \frac{1}{N_{\text{traj}}K} \sum_{i=1}^{N_{\text{traj}}} \sum_{k=0}^{K-1} \left( \lambda_{\text{rec}} \|\mathcal{D}(\mathcal{E}(\mathbf{x}_k^{(i)})) - \mathbf{x}_k^{(i)}\|_2^2 \right. \\ & + \lambda_{\text{pred}} \|\mathcal{D}(\mathbf{A}\mathcal{E}(\mathbf{x}_k^{(i)})) - \mathbf{x}_{k+1}^{(i)}\|_2^2 \\ & + \lambda_{\text{latent}} \|\mathbf{A}\mathcal{E}(\mathbf{x}_k^{(i)}) - \mathcal{E}(\mathbf{x}_{k+1}^{(i)})\|_2^2 \Big) \\ (3.6) \quad & + \lambda_{\text{reg}} R(\mathbf{A}), \end{aligned}$$

where the regularization term

$$R(\mathbf{A}) = (\max\{0, \|\mathbf{A}\|_2 - 1\})^2$$

penalizes violations of a spectral norm constraint and promotes stability of the latent linear dynamics. The reconstruction term  $\|\mathcal{D}(\mathcal{E}(\mathbf{x}_k^{(i)})) - \mathbf{x}_k^{(i)}\|$  enforces that the encoder–decoder pair provides a faithful representation of the physical state, ensuring that essential structures are preserved when mapping between the physical and latent spaces. The prediction term  $\|\mathcal{D}(\mathbf{A}\mathcal{E}(\mathbf{x}_k^{(i)})) - \mathbf{x}_{k+1}^{(i)}\|$  encourages the decoded latent state, propagated linearly by  $\mathbf{A}$ , to reproduce the one-step evolution of the physical system. The latent consistency term  $\|\mathbf{A}\mathcal{E}(\mathbf{x}_k^{(i)}) - \mathcal{E}(\mathbf{x}_{k+1}^{(i)})\|$  aligns the linearly propagated latent variable with the encoded latent representation of the subsequent state, thereby enforcing coherence between the learned linear dynamics and the underlying nonlinear evolution. Together, these terms ensure that the latent variables evolve approximately linearly under a stable operator, a property that is crucial for reliable sequential filtering.

*Stage II: learning a consistent latent observation embedding.* After the latent dynamics have been identified, the encoder  $\mathcal{E}$ , decoder  $\mathcal{D}$ , and transition operator  $\mathbf{A}$  are kept fixed. In the second stage, an observation encoder  $\mathcal{E}_{\text{obs}}$  is trained to embed observations into the same latent coordinate system. We consider a linear observation model in the latent space and define the observation alignment loss

$$(3.7) \quad \mathcal{L}_{\text{obs}}(\mathcal{E}_{\text{obs}}) = \frac{1}{N_{\text{traj}}(K+1)} \sum_{i=1}^{N_{\text{traj}}} \sum_{k=0}^K \|\mathcal{E}_{\text{obs}}(\mathbf{y}_k^{(i)}) - \mathbf{H}\mathcal{E}(\mathbf{x}_k^{(i)})\|_2^2,$$

where  $\mathbf{H}$  denotes a prescribed linear observation operator in the latent space. In practice, a convenient and commonly used choice is  $\mathbf{H} = \mathbf{I}$ , in which case the observation

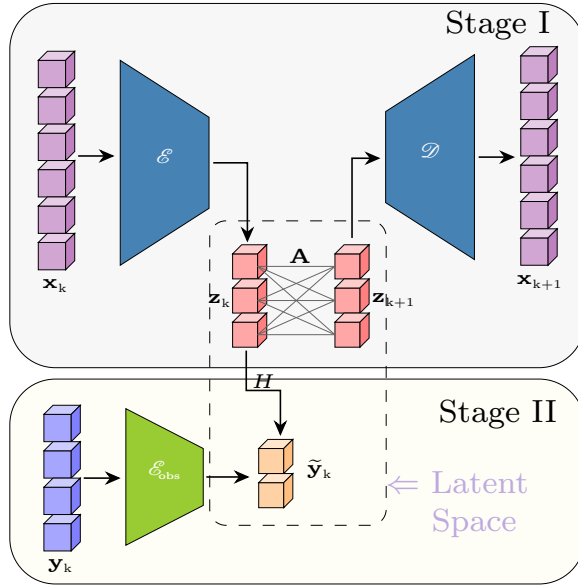


Fig. 1: The architecture of latent autoencoder framework. It consists of four principal trainable components: a state encoder  $\mathcal{E}$  that projects physical states into a compact latent space, a decoder  $\mathcal{D}$  that reconstructs physical states from latent representations, a linear transition operator  $\mathbf{A}$  that governs latent dynamics, and an observation encoder  $\mathcal{E}_{\text{obs}}$  that maps observations into the same latent manifold.

encoder directly maps measurements into the latent state space without introducing additional trainable parameters.

Through this two-stage training procedure, the LAE framework learns a stable latent linear dynamical system together with a consistent embedding of states and observations. The result is a closed linear state-space model in the latent variables, in which the assumptions underlying Kalman filtering are approximately satisfied. In the next subsection, we integrate the ensemble Kalman filter directly into this learned latent representation, leading to the proposed LAE-EnKF.

**3.3. Latent autoencoder ensemble Kalman filter.** Once training is completed, the learned latent dynamics and observation embeddings define a linear state-space model in the latent variables. The ensemble Kalman filter can therefore be applied directly in the latent space, where its structural assumptions are approximately satisfied.

In the proposed LAE-EnKF, the forecast step propagates latent ensemble members using the learned linear operator  $\mathbf{A}$ , while the analysis step performs Kalman-type updates using latent observations generated by  $\mathcal{E}_{\text{obs}}$ . The updated latent ensemble is then decoded to recover full-order state estimates in the physical space. A detailed algorithmic description is provided in Algorithm 3.1.

By shifting data assimilation from the nonlinear physical space to a compact latent space governed by stable linear dynamics, the LAE-EnKF preserves the scalability

---

**Algorithm 3.1** Latent Autoencoder Ensemble Kalman Filter (LAE-EnKF)
 

---

**Require:** Training data  $\{(\mathbf{x}_k, \mathbf{y}_k)\}$ ; initial physical ensemble  $\{\mathbf{x}_0^{(j)}\}_{j=1}^{N_e}$ .

**Ensure:** State estimates  $\{\hat{\mathbf{x}}_k\}$ , trained  $\mathcal{E}$ ,  $\mathcal{D}$ , transition matrix  $\mathbf{A}$ , and observation encoder  $\mathcal{E}_{\text{obs}}$ .

- 1: **Offline training (LAE model)**
- 2: Train  $(\mathcal{E}, \mathcal{D}, \mathbf{A})$  by minimizing the empirical latent loss  $\mathcal{L}_{\text{lat}}$  in (3.6).
- 3: Train  $\mathcal{E}_{\text{obs}}$  by minimizing the observation-alignment loss  $\mathcal{L}_{\text{obs}}$  in (3.7).
- 4: **Online assimilation (LAE-EnKF)**
- 5: **Initialization:**  $\hat{\mathbf{z}}_0^{(j)} = \mathcal{E}(\mathbf{x}_0^{(j)})$ ,  $j = 1, \dots, N_e$ .
- 6: **for**  $k = 1, 2, \dots, K$  **do**
- 7:   **Forecast step:**  $\hat{\mathbf{z}}_{k|k-1}^{(j)} = \mathbf{A}\hat{\mathbf{z}}_{k-1}^{(j)}$ ,  $j = 1, \dots, N_e$ .
- 8:   Compute latent observation:  $\hat{\mathbf{y}}_k^{(j)} = \mathbf{H}\mathbf{z}_{k|k-1}^{(j)}$ ,  $j = 1, \dots, N_e$ .
- 9:   Compute latent forecast mean:  $\bar{\mathbf{z}}_{k|k-1} = \frac{1}{N_e} \sum_{j=1}^{N_e} \hat{\mathbf{z}}_{k|k-1}^{(j)}$ .
- 10:   Compute latent observation mean:  $\bar{\mathbf{y}}_k = \frac{1}{N_e} \sum_{j=1}^{N_e} \hat{\mathbf{y}}_k^{(j)}$ .
- 11:   Compute empirical latent covariances:

$$\mathbf{P}_{zy} = \frac{1}{N_e - 1} \sum_{j=1}^{N_e} (\hat{\mathbf{z}}_{k|k-1}^{(j)} - \bar{\mathbf{z}}_{k|k-1})(\hat{\mathbf{y}}_k^{(j)} - \bar{\mathbf{y}}_k)^\top,$$

$$\mathbf{P}_{yy} = \frac{1}{N_e - 1} \sum_{j=1}^{N_e} (\hat{\mathbf{y}}_k^{(j)} - \bar{\mathbf{y}}_k)(\hat{\mathbf{y}}_k^{(j)} - \bar{\mathbf{y}}_k)^\top.$$

- 12:   Encode observation:  $\tilde{\mathbf{y}}_k = \mathcal{E}_{\text{obs}}(\mathbf{y}_k)$ .

- 13:   **Analysis step:**

$$\hat{\mathbf{z}}_k^{(j)} = \hat{\mathbf{z}}_{k|k-1}^{(j)} + \mathbf{P}_{zy}(\mathbf{P}_{yy} + \tilde{\Gamma})^{-1}(\tilde{\mathbf{y}}_k + \tilde{\boldsymbol{\eta}}_k^{(j)} - \hat{\mathbf{y}}_k^{(j)}), \quad j = 1, \dots, N_e.$$

- 14: **end for**

- 15: **Reconstruction:**  $\hat{\mathbf{x}}_k = \mathcal{D}\left(\frac{1}{N_e} \sum_{j=1}^{N_e} \hat{\mathbf{z}}_k^{(j)}\right)$ .
- 

and efficiency of the classical EnKF while avoiding the structural mismatch that limits its performance in nonlinear settings. This representation-driven approach provides a principled pathway for extending ensemble Kalman filtering to high-dimensional nonlinear systems.

**4. Theoretical Analysis.** In this section, we provide a performance guarantee of the proposed LAE. Our LAE is motivated by the manifold hypothesis [33, 21], which suggests that although the full-order states  $\mathbf{x} \in \mathbb{R}^D$  is high-dimensional, the set of dynamically attainable states concentrates on a low-dimensional geometric structure. In particular, we assume that the data lie on an  $n$ -dimensional compact smooth Riemannian manifold  $\mathcal{M}$  that is isometrically embedded in the ambient space  $\mathbb{R}^D$  [23]. The compactness of  $\mathcal{M}$  implies uniform boundedness, there exists  $B > 0$

such that

$$\|\mathbf{x}\|_\infty \leq B, \quad \forall \mathbf{x} \in \mathcal{M}.$$

Furthermore, we assume that the manifold  $\mathcal{M}$  admits a global smooth parametrization, so that it can be represented by a single coordinate system. This corresponds to the single-chart setting in the chart autoencoder framework of [25]. Within this framework, the encoder–decoder pair  $(\mathcal{E}, \mathcal{D})$  can be viewed as approximating a global chart and its inverse on  $\mathcal{M}$ , while the latent operator  $\mathbf{A}$  acts on a Euclidean representation of the underlying manifold.

To derive an upper bound on the generalization error for the LAE, we impose the following assumptions.

**ASSUMPTION 1.** *Let  $\mathcal{M} \subset \mathbb{R}^D$  be a compact  $n$ -dimensional  $C^2$  submanifold. Assume that  $\mathcal{M}$  admits a global bi-Lipschitz parameterization  $\varphi : \mathcal{M} \rightarrow [-\Lambda, \Lambda]^n$  with inverse  $\phi = \varphi^{-1} : \varphi(\mathcal{M}) \rightarrow \mathcal{M}$ . That is, there exist constants  $C_\varphi, C_\phi > 0$  such that for all  $\mathbf{v}_1, \mathbf{v}_2 \in \mathcal{M}$ ,*

$$C_\varphi^{-1} \|\mathbf{v}_1 - \mathbf{v}_2\|_2 \leq \|\varphi(\mathbf{v}_1) - \varphi(\mathbf{v}_2)\|_2 \leq C_\varphi \|\mathbf{v}_1 - \mathbf{v}_2\|_2,$$

and

$$\|\phi(\mathbf{z}_1) - \phi(\mathbf{z}_2)\|_2 \leq C_\phi \|\mathbf{z}_1 - \mathbf{z}_2\|_2, \quad \mathbf{z}_1, \mathbf{z}_2 \in \varphi(\mathcal{M}).$$

Furthermore, assume that the one-step dynamics  $\mathbf{F} : \mathcal{M} \rightarrow \mathbb{R}^D$  admits a latent linear representation, i.e., there exists a matrix  $\mathbf{A}^* \in \mathbb{R}^{n \times n}$  with  $\|\mathbf{A}^*\|_2 \leq \rho$  for a fixed constant  $\rho \leq 1$ , such that

$$\mathbf{F}(\mathbf{x}) = \phi(\mathbf{A}^* \varphi(\mathbf{x})), \quad \forall \mathbf{x} \in \mathcal{M}.$$

We assume that all physical states used for training satisfy  $\mathbf{x}_k \in \mathcal{M}$ . Although the trajectory  $\{\mathbf{x}_k\}$  is generated by an underlying time-dependent Markov process, we further assume that the sampling interval exceeds the mixing time of the dynamics so that statistical dependence across samples becomes negligible, while we remark that our learning result may hold even for non i.i.d. data source (see [11] and the references within). Under this standard assumption in learning theory for dynamical systems, the data may be treated as approximately independent for the purpose of deriving finite-sample generalization bounds.

**ASSUMPTION 2.** *Let  $\{(\mathbf{x}, \mathbf{x}^+)\}_{k=1}^N$  denote the input-target pairs, where  $\mathbf{x}_k^+ = \mathbf{F}(\mathbf{x}_k)$  represents the one-step evolution under the true dynamics. We assume that these pairs are sampled i.i.d. according to the stationary transition distribution:*

$$(4.1) \quad (\mathbf{x}, \mathbf{x}^+) \stackrel{i.i.d.}{\sim} \mathbb{P}_{X, X^+},$$

supported on  $\mathcal{M} \times \mathcal{M}$ .

For the loss function (3.6), the weights  $\lambda_{\text{rec}}, \lambda_{\text{pred}}, \lambda_{\text{latent}}, \lambda_{\text{reg}}$  are tuning parameters used in practice to balance the relative scales of reconstruction, one-step prediction, latent consistency, and stability regularization. For the theoretical analysis, these weights act only as positive multiplicative scalings of the loss terms and therefore affect the generalization bound only through the leading constant, without changing the convergence rate. Accordingly, in the theoretical part, we set

$\lambda_{\text{rec}} = \lambda_{\text{pred}} = \lambda_{\text{latent}} = \lambda_{\text{reg}} = 1$  and use the following simplified loss function:

$$(4.2) \quad \mathcal{L}_{\text{lat}}^{\text{POP}}(\mathcal{E}, \mathcal{D}, \mathbf{A}) := \mathbb{E}_{(\mathbf{x}, \mathbf{x}^+) \sim \mathbb{P}_{\mathbf{x}, \mathbf{x}^+}} \left[ \|\mathcal{D}(\mathbf{A}\mathcal{E}(\mathbf{x})) - \mathbf{F}(\mathbf{x})\|_2^2 + \|\mathcal{D}(\mathcal{E}(\mathbf{x})) - \mathbf{x}\|_2^2 + \|\mathbf{A}\mathcal{E}(\mathbf{x}) - \mathcal{E}(\mathbf{F}(\mathbf{x}))\|_2^2 + R(\mathbf{A}) \right].$$

Under these assumptions, we obtain the following finite-sample upper bound for the squared generalization error of the LAE.

**THEOREM 4.1.** *Suppose that Assumptions 1 and 2 hold. Let  $(\widehat{\mathcal{E}}, \widehat{\mathbf{A}}, \widehat{\mathcal{D}})$  denote a global minimizer of the empirical objective (3.6) with all  $\lambda \equiv 1$ . Assume that the encoder–decoder class has sufficient approximation capacity to realize a global smooth parametrization of the manifold  $\mathcal{M}$  and its inverse. Then the squared generalization error satisfies*

$$(4.3) \quad \mathbb{E}_{\mathcal{S}} \left[ \mathcal{L}_{\text{lat}}^{\text{POP}}(\widehat{\mathcal{E}}, \widehat{\mathcal{D}}, \widehat{\mathbf{A}}) \right] \leq CD^2 \log^2 DN^{-\frac{2}{n+2}} \log^4 N,$$

for some constant  $C > 0$  depending only on  $n, B, \Lambda, \rho$ , the Lipschitz constants of the parametrization maps, and the volume of  $\mathcal{M}$ .

A detailed proof is provided in Appendix A. Our analysis follows the general proof strategy developed for the single-chart autoencoder framework [25], where the three components of the population loss (4.2) are bounded separately. Compared with [25], our setting includes an additional latent linear evolution term  $\mathbf{A}$ , which introduces an extra intermediate factor of order  $\mathcal{O}(N^{-\frac{2}{n+2}})$  in the estimation error. However, this additional term does not affect the overall convergence rate. Consequently, the final squared generalization error remains  $\mathcal{O}(N^{-\frac{2}{n+2}} \log^4 N)$  matching the rate achieved in the single-chart autoencoder setting.

The following theorem provides a corresponding generalization bound for the observation encoder under similar architectural assumptions. For simplicity of exposition, we consider the latent observation operator is fixed to the identity, i.e.,  $\mathbf{H} = \mathbf{I}$ .

**THEOREM 4.2.** *Suppose that Assumption 1 holds, and that the pre-trained components  $\mathcal{E}, \mathcal{D}$ , and  $\mathbf{A}$  are fixed. Let  $\widehat{\mathcal{E}}_{\text{obs}}$  denote a global minimizer of the observation alignment objective (3.7). Assume that the observation encoder class has sufficient approximation capacity to represent the mapping  $\mathbf{y} \mapsto \mathcal{E}(\mathbf{x})$  of the data distribution induced by the observation process. Then the expected generalization error satisfies*

$$(4.4) \quad \mathbb{E}_{\mathcal{S}} \mathbb{E}_{(\mathbf{x}, \mathbf{y})} \left[ \|\widehat{\mathcal{E}}_{\text{obs}}(\mathbf{y}) - \mathcal{E}(\mathbf{x})\|_2^2 \right] \leq CD_y^2 \log^2 D_y N^{-\frac{2}{n+2}} \log^4 N,$$

for some constant  $C > 0$  depending only on  $n, B, \Lambda$ , and volume of the manifold  $\mathcal{M}$ .

The proof follows similar arguments as in Theorem 4.1 and is therefore omitted for brevity.

**5. Numerical Results.** In this section, we present numerical experiments to assess the performance of the proposed LAE-EnKF in nonlinear data assimilation problems. The experiments are designed to evaluate three key aspects of the method: assimilation accuracy, robustness over time, and the benefit of enforcing linear dynamics in a learned latent space. All of the following numerical examples are carried out on a computing server with a NVIDIA GeForce RTX 3090 GPU.

To enrich the information content of partial observations, we adopt a time-delay embedding strategy [32]. Specifically, a sequence of  $L$  consecutive observations is concatenated to form an augmented observation vector,

$$\mathbf{y}_k^{(L)} = [\mathbf{y}_{k-L+1}^\top, \dots, \mathbf{y}_{k-1}^\top, \mathbf{y}_k^\top]^\top,$$

which is then processed by the observation encoder  $\mathcal{E}_{\text{obs}}$ . This approach allows the latent observation embedding to exploit short-term temporal correlations without modifying the filtering formulation.

To quantify assimilation performance, we report several standard error metrics. The relative state error at time step  $k$  is defined as

$$(5.1) \quad e_{\text{Rel},k} = \frac{\|\widehat{\mathbf{x}}_k - \mathbf{x}_k\|_2}{\|\mathbf{x}_k\|_2},$$

where  $\widehat{\mathbf{x}}_k$  denotes the estimated state and  $\mathbf{x}_k$  is the reference solution. To measure overall accuracy over a finite time window, we further define the time-averaged root-mean-square error and the corresponding global relative error,

$$(5.2) \quad E_{1:T} = \sqrt{\frac{1}{TD} \sum_{k=1}^T \sum_{i=1}^D (\widehat{x}_{k,i} - x_{k,i})^2}, \quad E_{\text{Rel},1:T} = \frac{E_{1:T}}{\sqrt{\frac{1}{T} \sum_{k=1}^T \left( \frac{1}{D} \sum_{i=1}^D x_{k,i}^2 \right)}}.$$

Here,  $x_{k,i}$  and  $\widehat{x}_{k,i}$  denote the  $i$ th components of the true and estimated state vectors at time step  $k$ , respectively.

To highlight the role of the latent linear structure and latent-space filtering, we compare the proposed LAE-EnKF with the following baseline methods.

- (i) **EnKF**: the standard ensemble Kalman filter, where both forecast and analysis steps are carried out directly in the physical state space. Compared with other methods, the implementation of EnKF would require the usage of the forecast and observation models.
- (ii) **AE-EnKF**: an autoencoder-assisted EnKF that uses a nonlinear autoencoder for dimensionality reduction, but performs the Kalman update in the physical space and does not impose any structure on the latent dynamics.
- (iii) **DAE-EnKF**: a deep autoencoder-based latent assimilation method, in which the EnKF update is performed in a learned latent space and the latent dynamics are modeled by a general neural network without linear constraints. This setting is similar in spirit to [24]. To ensure a fair comparison, the encoder and decoder architectures are identical to those used in the proposed LAE framework.

All methods use the same ensemble size, data normalization, and training configuration to ensure comparability. In particular, all state variables and observations are normalized to zero mean and unit variance prior to training and assimilation. In all experiments, the encoder and decoder are implemented using convolutional neural networks (CNN), which are well suited for high-dimensional systems with spatial structure. The state encoder consists of three convolutional layers. Each layer uses a  $4 \times 4$  kernel with stride 2, progressively reducing the spatial resolution while extracting multiscale features. A fully connected layer with *LeakyReLU* activations (negative slope  $\alpha = 0.1$ ) then maps the resulting features to the latent variables. The decoder mirrors this architecture and reconstructs the physical state using transposed convolutional layers.

The latent linear transition operator  $\mathbf{A}$  is learned as a single fully connected neural network without any activation function. This architectural choice explicitly enforces linear latent dynamics and is essential for maintaining structural compatibility with Kalman filtering. The observation encoder is implemented as a lightweight network composed of two one-dimensional convolutional layers with kernel size 3, followed by a fully connected layer that projects the observations into the latent space. This design allows observations with different spatial layouts to be embedded consistently with the latent state representation. The loss weights in (3.6) are selected so that the reconstruction, prediction, latent consistency, and regularization terms contribute at comparable magnitudes during training. All networks are implemented in PyTorch and trained using the Adam optimizer with an initial learning rate of  $10^{-3}$ . Early stopping based on the validation RMSE is applied to mitigate overfitting.

**5.1. Toy example.** We first consider a 100-dimensional nonlinear dynamical system that provides a controlled setting for examining the role of latent linear structure in data assimilation. Although the observed state is high dimensional, the underlying dynamics are intrinsically low dimensional, making this example well suited for assessing representation quality, latent dynamics, and filtering performance.

The system is governed by a single angular variable  $\theta_t$ , while the physical state is defined as

$$(5.3) \quad \mathbf{x}_t = W \begin{bmatrix} \cos(\theta_t) \\ \sin(\theta_t) \end{bmatrix} \in \mathbb{R}^{100}, \quad W \in \mathbb{R}^{100 \times 2}, \quad W_{ij} \sim \mathcal{N}(0, 1),$$

which embeds a two-dimensional rotational motion into a 100-dimensional ambient space. The angular dynamics evolve according to

$$(5.4) \quad \theta_{t+1} = \theta_t + \delta + \alpha \sin(2\theta_t) + c \epsilon_t,$$

where  $\delta = \pi/50$  is a constant rotation increment,  $\alpha = 0.01$  introduces weak nonlinearity,  $c = 0.01$  scales the process noise, and  $\epsilon_t \sim \mathcal{N}(0, 1)$ .

Observations are generated through a linear measurement model,

$$(5.5) \quad \mathbf{y}_t = H \mathbf{x}_t + \boldsymbol{\eta}_t, \quad \boldsymbol{\eta}_t \sim \mathcal{N}(0, 0.1^2),$$

where  $H \in \mathbb{R}^{2 \times 100}$  randomly selects two state components. We simulate  $N_{\text{traj}} = 500$  independent trajectories of length  $T = 100$ , with initial angles  $\theta_0$  sampled uniformly from  $[-\pi, \pi]$ . The data are split into 90% for training and 10% for testing.

To isolate the effect of enforcing linear latent dynamics, we first examine the geometric structure of the latent representations learned by the proposed LAE and by the DAE-EnKF model, referred to here as DAE for brevity. Fig. 2 shows the latent variables for latent dimensions  $n = 2, 3, 4$ . The DAE produces distorted closed curves, indicating that the learned latent dynamics do not preserve the underlying rotational structure. In contrast, the LAE generates significantly smoother latent trajectories, indicating that the imposed linear evolution promotes more regular and coherent temporal behavior in the latent space. When the latent dimension exceeds the intrinsic dimension ( $n = 3, 4$ ), we project the latent variables onto their first two principal components for visualization. In all cases, the LAE yields nearly isotropic circles in the projected space, showing that redundant latent coordinates are effectively suppressed. Fig. 3 further displays pairwise latent coordinates  $(z_i, z_j)$  for  $n = 3$ . Each pair forms an ellipse, confirming that all latent variables evolve coherently within a shared two-dimensional linear subspace. Together, these results indicate that the LAE

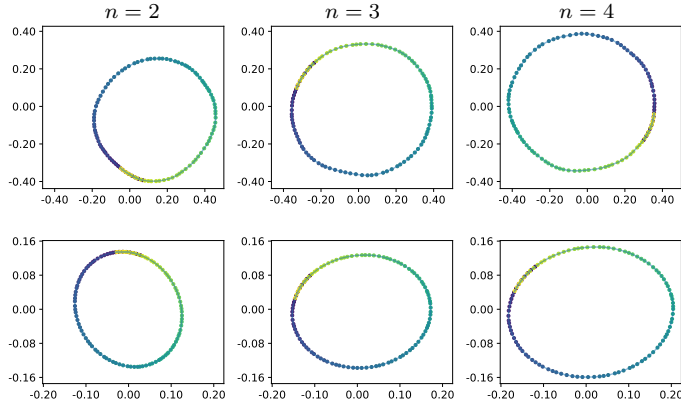


Fig. 2: Learned latent representations for latent dimensions  $n = 2, 3, 4$ . Top: latent variables learned by the autoencoder component of DAE-EnKF (denoted as DAE), where no structural constraint is imposed on the latent dynamics. Bottom: latent variables learned by the proposed LAE, which enforces linear evolution in the latent space. For  $n > 2$ , the latent variables are projected onto their first two principal components using PCA for visualization.

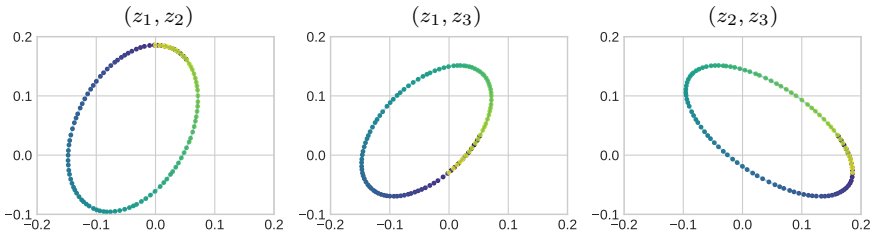


Fig. 3: Pairwise latent coordinate plots  $(z_i, z_j)$  for  $n = 3$  learned by the LAE.

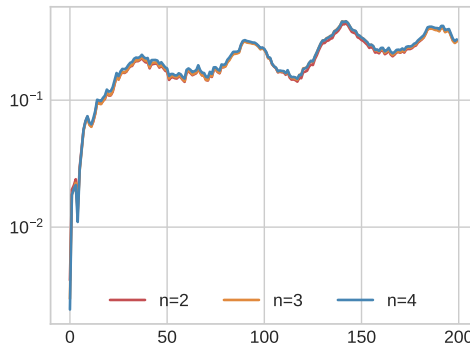


Fig. 4: Long-term prediction relative error for latent dimensions  $n = 2, 3, 4$ . Predictions are obtained by recursively propagating the learned latent dynamics forward in time and decoding back to the physical space.

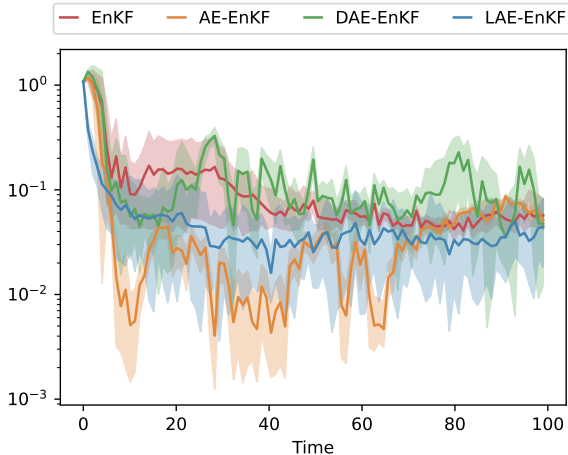


Fig. 5: Time evolution of the relative RMSE for different methods with latent dimension  $n = 2$ . Solid curves show the mean over 10 independent runs, and shaded regions indicate the corresponding 95% confidence intervals.

preserves the intrinsic manifold structure while enforcing global linear consistency in the latent dynamics.

We next study the impact of latent dimension on long-term prediction. Fig. 4 reports the relative prediction error obtained by propagating the learned latent dynamics forward in time and decoding back to the physical space. For latent dimensions  $n = 2, 3, 4$ , the prediction errors follow very similar trajectories over the entire forecast horizon, indicating that the long-term accuracy is only weakly affected by the choice of  $n$ . Although the underlying system is intrinsically two-dimensional, slightly higher-dimensional latent spaces do not degrade the prediction performance. These observations highlight an important feature of the proposed method: once the latent dimension is sufficient to represent the essential dynamics, the enforced linear structure prevents spurious modes from destabilizing long-term predictions. As a result, the method is both dimension-efficient and robust, achieving accurate predictions without requiring careful tuning of the latent dimension.

Finally, we evaluate data assimilation performance using LAE-EnKF and compare it with EnKF, AE-EnKF, and DAE-EnKF. Tab. 1 reports the global relative RMSE  $E_{\text{Rel},1:T}$  for latent dimensions  $n = 2, 3, 4$ . Fig. 5 shows the time evolution of the reconstruction error for  $n = 2$ , together with 95% confidence intervals over ten independent runs. While all learned-model-based methods outperform the standard EnKF, AE-EnKF and DAE-EnKF exhibit noticeable temporal fluctuations. In contrast, LAE-EnKF produces smoother and more stable error trajectories.

Fig. 6 compares reconstructed state trajectories in representative coordinate pairs  $(x_i, x_j)$ . The standard EnKF and DAE-EnKF deviate significantly from the true orbit. AE-EnKF better captures the overall geometry but still show intermittent departures. The LAE-EnKF reconstruction remains closely aligned with the true trajectory, yielding smoother and more coherent state evolution. These results demonstrate that enforcing linear latent dynamics improves both predictive stability and assimilation robustness, directly supporting the design motivation of the proposed LAE-EnKF.

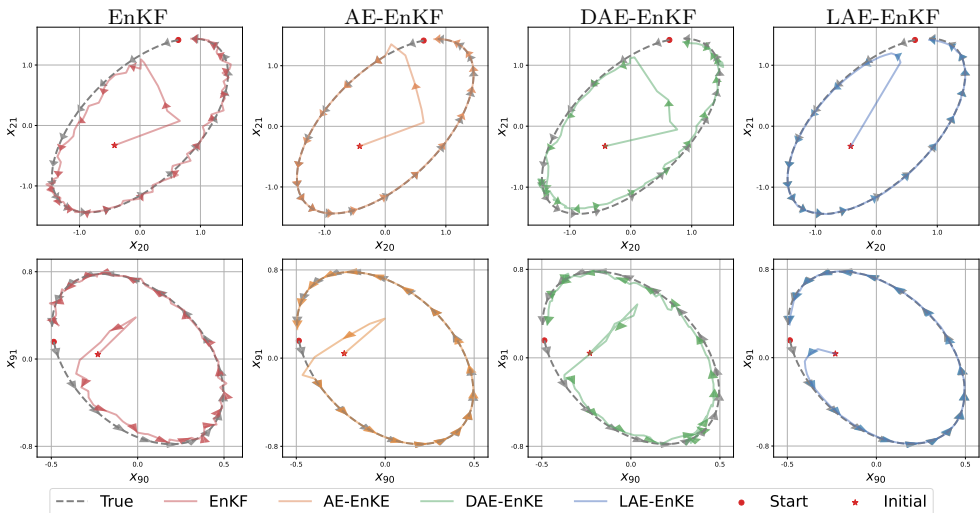


Fig. 6: Reconstructed state trajectories in two representative coordinate pairs  $(x_i, x_j)$  from the  $D = 100$  dimensional physical state for different methods with  $n = 2$ , compared with the true trajectory. Red stars indicate the initial reconstructed state, and red dots denote the initial true state.

Table 1: Relative error  $E_{\text{Rel},1:T}$  for different methods with various values of  $n$ .

$n$	EnKF	AE-EnKF	DAE-EnKF	LAE-EnKF
–	1.9757E-01	–	–	–
$n = 2$	–	1.6412E-01	2.3312E-01	<b>3.8947E-02</b>
$n = 3$	–	1.8667E-01	2.1106E-01	<b>1.4244E-02</b>
$n = 4$	–	1.9632E-01	4.0424E-01	<b>1.5682E-02</b>

**5.2. Advection–diffusion–reaction equation.** We consider a nonlinear advection diffusion reaction equation on the two-dimensional spatial domain  $\mathbf{x} = (x_1, x_2) \in [0, 1] \times [0, 1]$ ,

$$(5.6) \quad \begin{aligned} \partial_t u(\mathbf{x}, t) + \mathbf{v}(\mathbf{x}) \cdot \nabla u(\mathbf{x}, t) &= \mu \Delta u(\mathbf{x}, t) - \alpha (\sin u(\mathbf{x}, t) - u(\mathbf{x}, t)), \\ u(\mathbf{x}, 0) &= u_0(\mathbf{x}), \end{aligned}$$

subject to periodic boundary conditions. The diffusion coefficient and reaction parameter are set to  $\mu = 10^{-3}$  and  $\alpha = 0.8$ , respectively. The advection velocity field is given by

$$\mathbf{v}(\mathbf{x}) = (\sin(2\pi x_2), \sin(2\pi x_1)).$$

The initial condition is modeled as a zero-mean periodic Gaussian random field,

$$(5.7) \quad u(\mathbf{x}, 0) \sim \mathcal{GP}(0, K_\ell(\mathbf{x}, \mathbf{x}')),$$

with covariance kernel

$$K_\ell(\mathbf{x}, \mathbf{x}') = \exp\left(-\frac{\sin^2(\pi(x_1 - x_1')) + \sin^2(\pi(x_2 - x_2'))}{2\ell^2}\right).$$

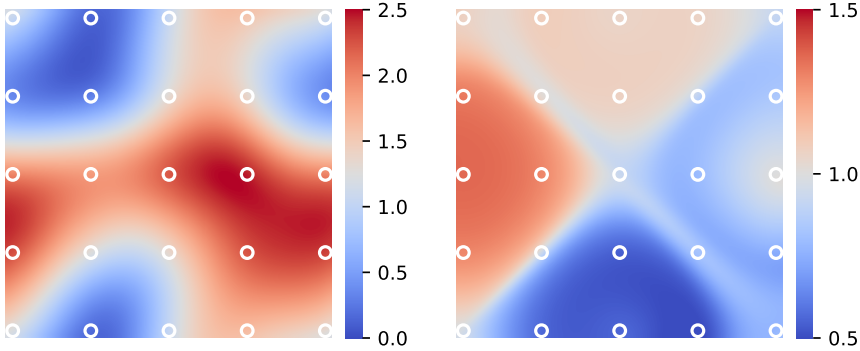


Fig. 7: True solution fields of the advection–diffusion–reaction equation at the initial time and final time  $T$ . White circles indicate the observation locations.

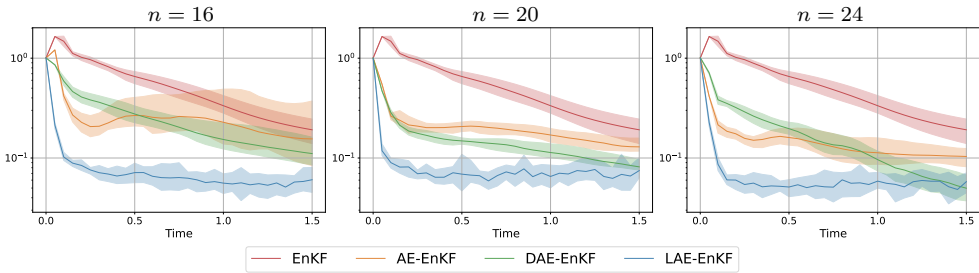


Fig. 8: Time evolution of the relative RMSE for Example 2 under latent dimensions  $n = 16, 20, 24$ . Solid curves indicate the mean over 10 independent runs, and the shaded regions represent the corresponding 95% confidence intervals.

Data assimilation is performed using sparse and noisy observations of the true solution. Measurements are collected at  $5 \times 5$  uniformly distributed sensor locations, resulting in an observation vector  $\mathbf{y}_k \in \mathbb{R}^{25}$ . Observations are available every  $\Delta t = 0.05$  up to the final time  $T = 1.5$ . Fig. 7 shows the true solution at the initial and final times, with sensor locations marked by white circles. The observation model is

$$(5.8) \quad \mathbf{y}_k = \mathbf{y}_k^{\text{true}} + \boldsymbol{\eta}_k, \quad \boldsymbol{\eta}_k \sim \mathcal{N}(\mathbf{0}, \sigma^2 \mathbf{I}),$$

where the noise level is set to  $\sigma = 0.01$ . The initial ensemble is generated by sampling spatial white noise followed by convolution with a two-dimensional Gaussian filter with standard deviation 3. This procedure introduces spatial correlation and provides a common prior ensemble for all filtering methods.

To study the effect of the latent dimension, we train LAE models with latent dimensions  $n \in \{16, 20, 24\}$  and apply the corresponding LAE-EnKF. Each experiment is repeated over ten independent runs. Fig. 8 reports the time evolution of the relative RMSE, where solid lines denote the mean and shaded regions indicate 95% confidence intervals. For all latent dimensions considered, LAE-EnKF achieves the lowest error and exhibits the most stable temporal behavior.

To further assess the quality of the reconstructed states, we examine the spatial structure of the assimilated solutions. Fig. 9 shows the reconstructed solution fields

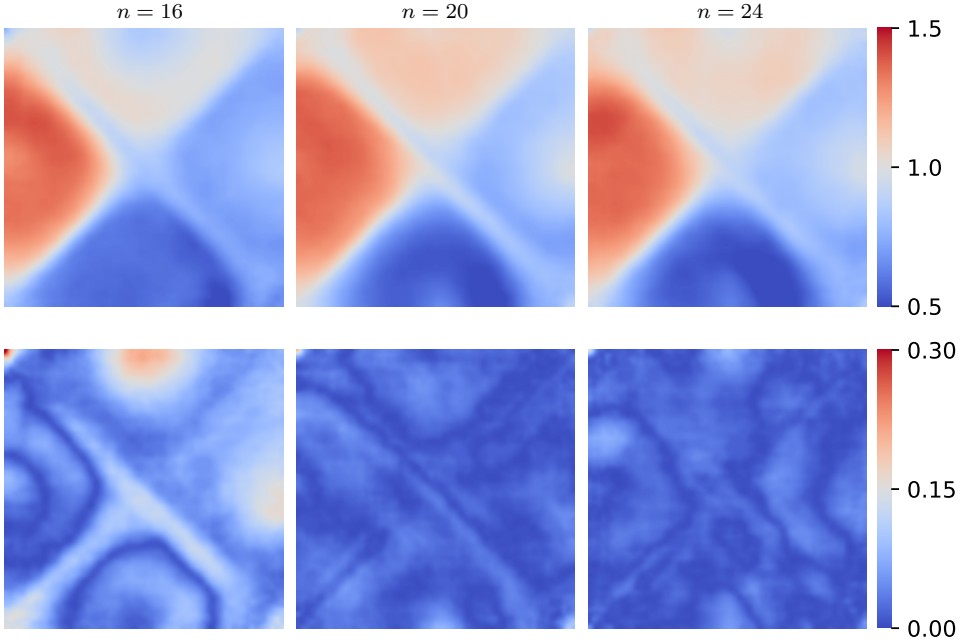


Fig. 9: Reconstructed fields and corresponding pointwise absolute error at the final time  $T$  by LAE-EnKF for different latent dimensions  $n = 16$ ,  $n = 20$ , and  $n = 24$ .

Table 2: Relative error  $E_{\text{Rel},1:T}$  and online computation time for Example 2.

$\sigma$	EnKF	AE-EnKF	DAE-EnKF	LAE-EnKF
$\sigma = 0.10$	0.6885	0.3468	0.4130	<b>0.1091</b>
$\sigma = 0.05$	0.6705	0.2988	0.3024	<b>0.0810</b>
$\sigma = 0.01$	0.5119	0.2142	0.2213	<b>0.0717</b>
<b>Time (s)</b>	1174.10	3.77	0.05	<b>0.04</b>

produced by LAE-EnKF at the final time  $T$ , together with the corresponding pointwise absolute errors, for different latent dimensions. Fig. 10 compares the reconstruction results of all methods for a representative case with  $n = 20$ . In all cases, LAE-EnKF more accurately recovers the dominant spatial patterns and provides smoother reconstructions in regions without direct observations.

Finally, Tab. 2 summarizes the global relative RMSE  $E_{\text{Rel},1:T}$  under different observation noise levels, together with the online computation time of the EnKF assimilation step. The results show that LAE-EnKF consistently achieves the best accuracy–efficiency trade-off. Compared with the standard EnKF, the proposed method substantially reduces computational cost while improving reconstruction accuracy. These results confirm that learning a stable linear latent representation and performing EnKF in the latent space can significantly enhance data assimilation performance for nonlinear PDE systems.

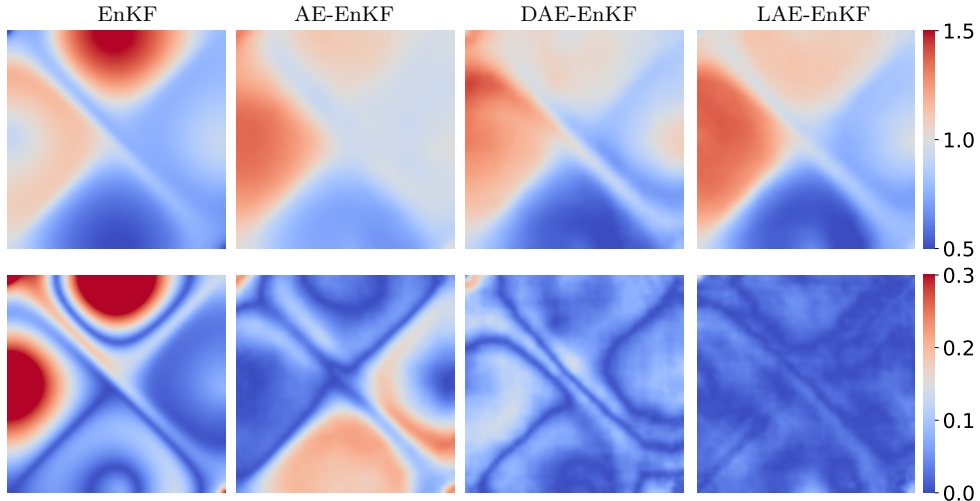


Fig. 10: Comparison of reconstructed fields and corresponding pointwise absolute error at the final time  $T$  for latent dimension  $n = 20$ .

**5.3. Lorenz–96 model.** We consider the chaotic Lorenz–96 system,

$$(5.9) \quad \frac{dx_i}{dt} = (x_{i+1} - x_{i-2})x_{i-1} - x_i + F, \quad i = 0, \dots, D-1,$$

with periodic boundary conditions  $x_D \equiv x_0$ ,  $x_{-1} \equiv x_{D-1}$ , and  $x_{-2} \equiv x_{D-2}$ . In all experiments, we set  $D = 40$  and the forcing parameter  $F = 8$ , which is a standard configuration that produces sustained chaotic dynamics. The system is integrated using a fourth-order Runge–Kutta scheme with time step 0.01.

Observations are generated according to

$$\mathbf{y}_k = \mathcal{H}(\mathbf{x}(t_k)) + \boldsymbol{\eta}_k, \quad \boldsymbol{\eta}_k \sim \mathcal{N}(\mathbf{0}, \sigma^2 \mathbf{I}),$$

where  $\mathcal{H}$  is a linear subsampling operator that extracts every other state variable,

$$\mathcal{H}(\mathbf{x}) = (x_0, x_2, \dots, x_{38})^\top,$$

and the observation noise level is set to  $\sigma = 1$ . This setup represents a partially observed scenario in which only half of the state variables are directly measured.

*Dense observation regime.* We first consider a relatively dense observation setting with observations available every  $\Delta t = 0.1$ . LAE models are trained with latent dimensions  $n \in \{64, 80, 100\}$ , and the resulting LAE-EnKF is compared with AE-EnKF, DAE-EnKF, and an EnKF baseline. Tab. 3 reports the the global relative RMSE  $E_{\text{Rel},1:T}$  over the full state.

For reference, we report results for the standard EnKF both with and without covariance localization. As is well known for the Lorenz–96 system, the EnKF without localization suffers from severe sampling errors and produces extremely poor assimilation results. Without localization, spurious long-range correlations dominate the analysis step, leading to filter instability and large reconstruction errors. For this reason, unless otherwise stated, all subsequent references to EnKF correspond to the localized EnKF implementation. In contrast, all three latent-space methods—AE-EnKF,

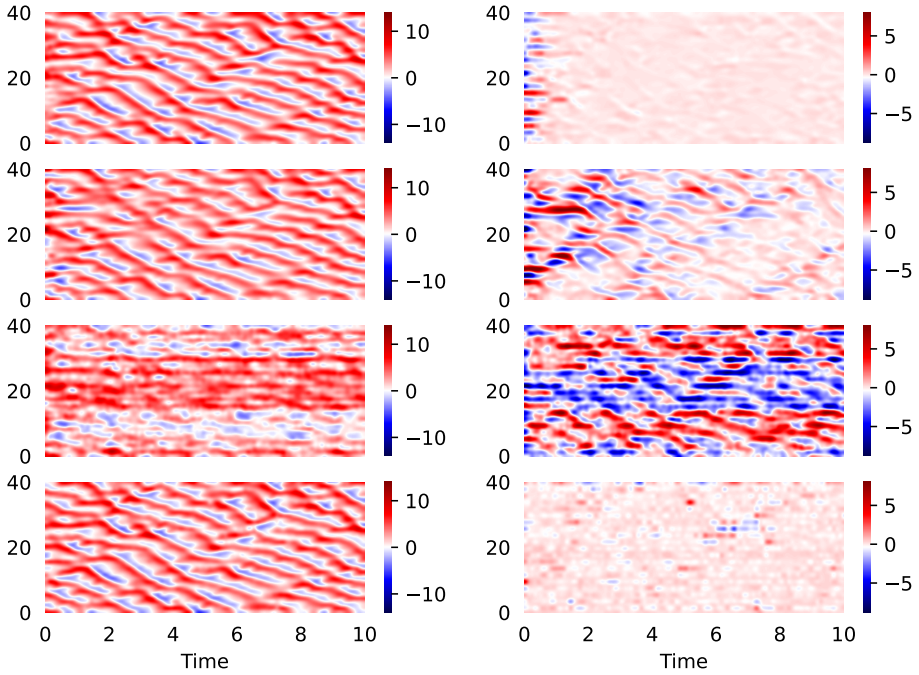


Fig. 11: Reconstructed spatial state fields (Left) and corresponding error (Right) with the observation interval  $\Delta t = 0.1$  and latent dimension  $n = 64$ . From top to bottom, the results show the localization EnKF, AE-EnKF, DAE-EnKF and the LAE-EnKF.

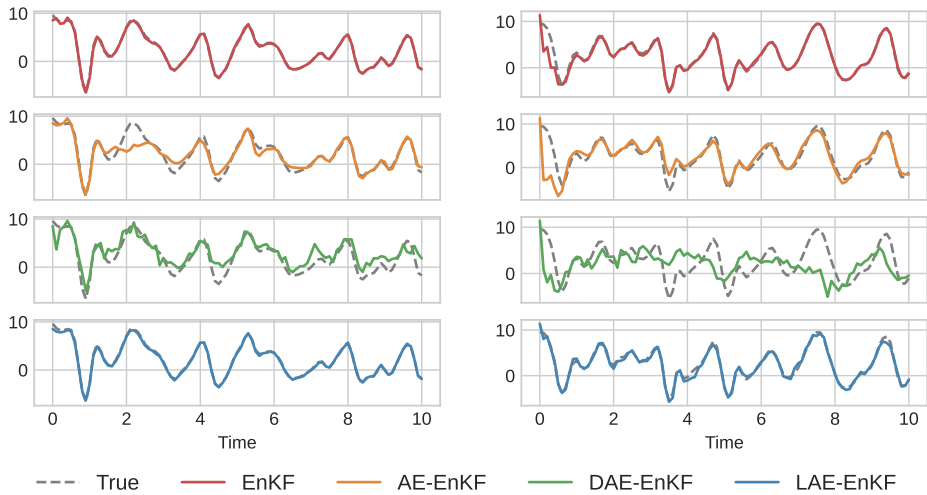


Fig. 12: Time evolution of a representative observed variable (Left) and an unobserved variable (Right) reconstructed with observation interval  $\Delta t = 0.1$  and latent dimension  $n = 64$ , compared with the corresponding true trajectories. From top to bottom, the results show the localization EnKF, AE-EnKF, DAE-EnKF and the LAE-EnKF.

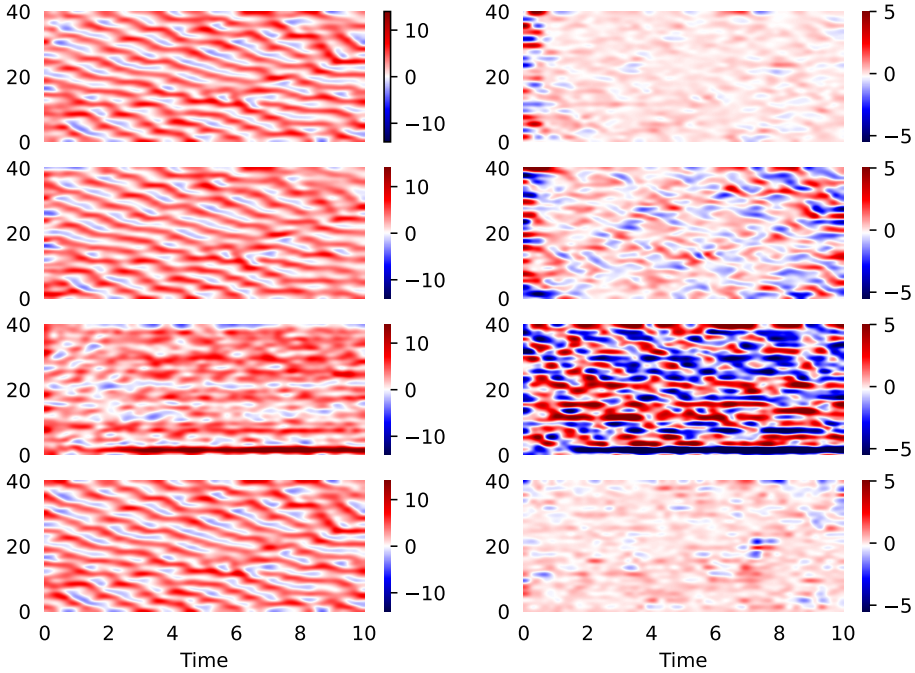


Fig. 13: Reconstructed spatial state fields (Left) and corresponding error (Right) with the observation interval  $\Delta t = 0.2$  and latent dimension  $n = 64$ . From top to bottom, the results show the localization EnKF, AE-EnKF, DAE-EnKF and the LAE-EnKF.

DAE-EnKF, and the proposed LAE-EnKF—are implemented using the standard EnKF formulation without covariance localization. This choice is intentional and highlights a key distinction: the latent-space representations are designed to mitigate sampling errors through structured dynamics, rather than through ad hoc localization techniques.

Fig. 11 shows the reconstructed spatial fields and the corresponding errors for the representative case  $n = 64$ , while Fig. 12 presents the temporal evolution of one observed and one unobserved state variable. AE-EnKF and DAE-EnKF exhibit larger reconstruction errors and irregular temporal behavior, indicating instability in the learned latent dynamics. In contrast, LAE-EnKF consistently achieves lower errors and smoother temporal evolution for both observed and unobserved variables. This demonstrates that enforcing stable linear dynamics in the latent space substantially improves the recovery of hidden states in a chaotic system.

*Sparse observation regime.* We next consider a sparser observation setting with the observation interval increased to  $\Delta t = 0.2$ . The same latent dimensions  $n \in \{64, 80, 100\}$  are used for all learned-model-based methods to ensure a fair comparison. The corresponding error metrics are again reported in Tab. 3. Fig. 13 shows the reconstructed spatial fields and errors for  $n = 64$ . Despite the reduced observation frequency, LAE-EnKF maintains reconstruction accuracy comparable to that obtained with  $\Delta t = 0.1$ , demonstrating strong robustness to observation sparsity.

Fig. 14 shows the temporal evolution of one observed and one unobserved variable

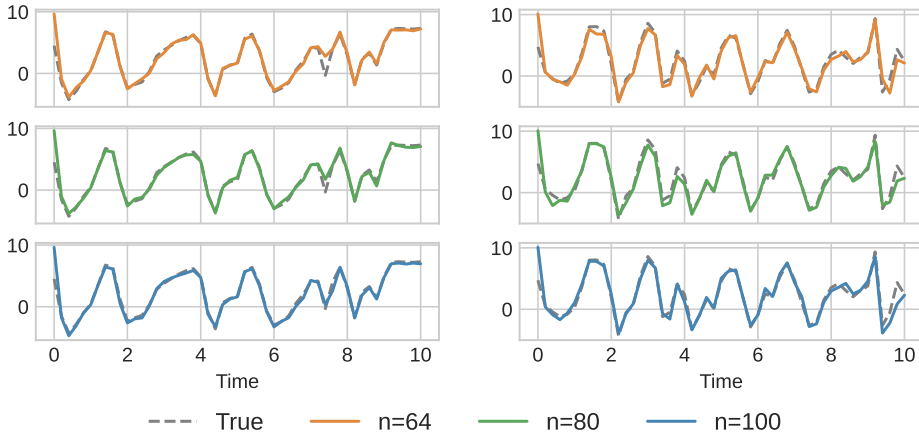


Fig. 14: Time evolution of a representative observed variable (Left) and an unobserved variable (Right) reconstructed by LAE-EnKF with observation interval  $\Delta t = 0.2$  for different latent dimension  $n = 64, 80, 100$ .

Table 3: Relative RMSE  $E_{\text{Rel},1:T}$  for different methods with varying latent dimension  $n$  under two observation intervals.

		$n$	EnKF		AE- EnKF	DAE- EnKF	LAE- EnKF
			w/o loc.	w/ loc.			
$\Delta t = 0.1$	-	-	0.5305	0.1512	-	-	-
	$n = 64$	-	-	-	0.4584	0.8837	<b>0.1477</b>
	$n = 80$	-	-	-	0.4940	0.7523	<b>0.1512</b>
	$n = 100$	-	-	-	0.3998	0.7254	<b>0.1429</b>
$\Delta t = 0.2$	-	-	0.3698	0.1697	-	-	-
	$n = 64$	-	-	-	0.3733	1.1631	<b>0.1585</b>
	$n = 80$	-	-	-	0.3092	0.7142	<b>0.1605</b>
	$n = 100$	-	-	-	0.3225	0.6590	<b>0.1531</b>

reconstructed by LAE-EnKF. As the latent dimension increases, the reconstruction of the observed variable improves steadily, while the unobserved variable is accurately captured across all tested dimensions. This behavior indicates that the learned linear latent dynamics provide reliable temporal extrapolation and support stable assimilation under infrequent observations.

Overall, the Lorenz-96 experiments show that the proposed LAE-EnKF captures the essential dynamics of a chaotic system within a compact linear latent representation. By enabling stable and accurate data assimilation under partial and sparse observations, the LAE-EnKF extends the applicability of ensemble Kalman filtering to nonlinear chaotic systems in a fully data-driven setting.

**6. Conclusion.** This paper introduced the latent autoencoder ensemble Kalman filter (LAE-EnKF), a structure-preserving framework for data assimilation in nonlinear and partially observed systems. By learning a nonlinear encoder–decoder pair together with a stable linear latent dynamical model and a unified observation embedding, the proposed approach constructs a latent representation in which the assumptions underlying Kalman filtering are approximately satisfied. This design enables ensemble Kalman filtering to be performed directly in the learned latent space, mitigating the structural mismatch that often limits the performance of standard EnKF in strongly nonlinear regimes. Extensive experiments on representative nonlinear and chaotic systems showed that the LAE-EnKF consistently improves assimilation accuracy, robustness, and long-term stability compared with the classical EnKF and existing autoencoder-assisted methods, while maintaining favorable computational efficiency.

The proposed framework opens several promising directions for future research. These include extensions to systems with model error and parameter uncertainty, adaptive latent dimension selection, and integration with localization and inflation strategies for large-scale geophysical applications. More broadly, this work highlights the potential of structure-aware representation learning as a principled pathway for advancing ensemble-based data assimilation in complex nonlinear systems.

**Appendix A. Proof of Theorem 4.1.** To prove Theorem 4.1, we follow the proof strategy developed in [25], which establishes covering number bounds for deep ReLU networks when approximating functions supported on low-dimensional manifolds. Our proof adopts the same notation and technical framework, with adaptations tailored to the present setting.

We denote by  $\mathcal{F}_{\text{NN}}(d_1, d_2; L, p, K, \kappa, R)$  the class of neural networks introduced in [25], where  $d_1$  and  $d_2$  are the input and output dimensions. The networks have depth  $L$ , width  $p$ , and at most  $K$  nonzero parameters, each bounded by  $\kappa$  in magnitude. The effective parameter count  $K$  may depend on  $(d_1, d_2)$ . For inputs satisfying  $\|\mathbf{x}\|_\infty \leq B$ , the network outputs are uniformly bounded by  $R$ . The proof is based on controlling both approximation and estimation errors through a covering number bound for the class  $\mathcal{F}_{\text{NN}}$  under the uniform norm. To make the argument precise, we first introduce the assumptions and auxiliary lemmas needed for the subsequent analysis.

**DEFINITION A.1** (Covering number [35, Definition 2.1.5]). *For any  $\delta > 0$ , the covering number of  $\mathcal{F}$  is defined as*

$$\mathcal{Q}(\delta, \mathcal{F}, \|\cdot\|) = \min \{|\mathcal{S}| : \mathcal{S} \text{ is a } \delta\text{-cover of } \mathcal{F} \text{ under } \|\cdot\|\}.$$

**LEMMA A.2** ([12, Lemma 5.3]). *Assume that the input domain satisfies  $\|\mathbf{x}\|_\infty \leq B$ . For any  $\delta > 0$ ,*

$$(A.1) \quad \mathcal{Q}(\delta, \mathcal{F}_{\text{NN}}(d_1, d_2; L, p, K, \kappa, R), \|\cdot\|_{L^\infty, \infty}) \leq \left( \frac{2L^2(pB + 2)\kappa^L p^{L+1}}{\delta} \right)^K.$$

We also define the class of linear latent dynamics:

$$\mathcal{F}_{\text{Lin}}^A := \{z \mapsto \mathbf{A}z \mid \mathbf{A} \in \mathbb{R}^{n \times n}, \|\mathbf{A}\|_2 \leq \rho\},$$

where  $0 < \rho \leq 1$  is a fixed constant.

**LEMMA A.3.** *Suppose Assumption 1 holds. For any  $0 < \varepsilon < 1$ , there exist  $\tilde{\mathcal{E}} \in \mathcal{F}_{\text{NN}}^\mathcal{E} = \mathcal{F}(D, n; L_\mathcal{E}, p_\mathcal{E}, K_\mathcal{E}, \kappa_\mathcal{E}, R_\mathcal{E})$ ,  $\tilde{\mathbf{A}} \in \mathbb{R}^{n \times n}$  with  $\|\tilde{\mathbf{A}}\|_2 \leq \rho$  and  $\tilde{\mathcal{D}} \in \mathcal{F}_{\text{NN}}^\mathcal{D} = \mathcal{F}(n, D; L_\mathcal{D}, p_\mathcal{D}, K_\mathcal{D}, \kappa_\mathcal{D}, R_\mathcal{D})$  such that*

$$(A.2) \quad \sup_{\mathbf{x} \in \mathcal{M}} \left\| \tilde{\mathcal{D}}(\tilde{\mathbf{A}}\tilde{\mathcal{E}}(\mathbf{x})) - \mathbf{F}(\mathbf{x}) \right\|_\infty \leq \varepsilon.$$

*Proof.* By [16, Theorem 2.2], for any  $0 < \varepsilon < 1$ , let  $\varepsilon_1 = \frac{\varepsilon}{(1+C_\phi\rho\sqrt{n})} < 1$ , there exists an encoder network  $\tilde{\mathcal{E}}$  such that

$$\sup_{\mathbf{x} \in \mathcal{M}} \|\tilde{\mathcal{E}}(\mathbf{x}) - \varphi(\mathbf{x})\|_\infty \leq \varepsilon_1.$$

Moreover, by Kirszbraun's theorem [22], the inverse map  $\phi = \varphi^{-1}$  admits a Lipschitz extension (still denoted by  $\phi$ ) to  $[-\Lambda, \Lambda]^n$  with Lipschitz constant  $C_\phi$ . Applying the approximation result of [38, Lemma 8] to this extended  $\phi$ , there exists a decoder network  $\tilde{\mathcal{D}}$  such that

$$\sup_{\mathbf{z} \in [-\Lambda, \Lambda]^n} \|\tilde{\mathcal{D}}(\mathbf{z}) - \phi(\mathbf{z})\|_\infty \leq \varepsilon_1.$$

Set  $\tilde{\mathbf{A}} = \mathbf{A}^*$ . For any  $\mathbf{x} \in \mathcal{M}$ , letting  $u = \mathbf{A}^* \tilde{\mathcal{E}}(\mathbf{x})$  and  $v = \mathbf{A}^* \varphi(\mathbf{x})$ , we have

$$\|\tilde{\mathcal{D}}(u) - \mathbf{F}(\mathbf{x})\|_\infty = \|\tilde{\mathcal{D}}(u) - \phi(v)\|_\infty \leq \|\tilde{\mathcal{D}}(u) - \phi(u)\|_\infty + \|\phi(u) - \phi(v)\|_\infty.$$

Using Lipschitz continuity of  $\phi$ , we obtain

$$\|\phi(u) - \phi(v)\|_\infty \leq \|\phi(u) - \phi(v)\|_2 \leq C_\phi \|\mathbf{A}^*\|_2 \|\tilde{\mathcal{E}}(\mathbf{x}) - \varphi(\mathbf{x})\|_2 \leq C_\phi \rho \sqrt{n} \varepsilon_1.$$

Hence

$$\sup_{\mathbf{x} \in \mathcal{M}} \|\tilde{\mathcal{D}}(\mathbf{A}^* \tilde{\mathcal{E}}(\mathbf{x})) - \mathbf{F}(\mathbf{x})\|_\infty \leq \varepsilon. \quad \square$$

We now present the proof of Theorem 4.1.

*Proof of Theorem 4.1.* To simplicity the notations, for any given  $\mathcal{F}_{\text{NN}}^\mathcal{E}$ ,  $\mathcal{F}_{\text{Lin}}^A$  and  $\mathcal{F}_{\text{NN}}^\mathcal{D}$ , we define the network class

$$\begin{aligned} \mathcal{F}_{\text{NN}}^\mathcal{G} &= \{\mathcal{G} = \mathcal{D} \circ \mathbf{A} \circ \mathcal{E} \mid \mathcal{D} \in \mathcal{F}_{\text{NN}}^\mathcal{D}, \mathbf{A} \in \mathcal{F}_{\text{Lin}}^A, \mathcal{E} \in \mathcal{F}_{\text{NN}}^\mathcal{E}\}, \\ \mathcal{F}_{\text{AE}}^\mathcal{H} &= \{\mathcal{H} = \mathbf{A} \circ \mathcal{E} \mid \mathbf{A} \in \mathcal{F}_{\text{Lin}}^A, \mathcal{E} \in \mathcal{F}_{\text{NN}}^\mathcal{E}\}, \\ \mathcal{F}_{\text{NN}}^{\mathcal{D}\mathcal{E}} &= \{\mathcal{D}\mathcal{E} = \{\mathcal{D} \circ \mathcal{E} \mid \mathcal{D} \in \mathcal{F}_{\text{NN}}^\mathcal{D}, \mathcal{E} \in \mathcal{F}_{\text{NN}}^\mathcal{E}\}\}, \end{aligned}$$

and denote  $\widehat{\mathcal{G}} = \widehat{\mathcal{D}} \circ \widehat{\mathbf{A}} \circ \widehat{\mathcal{E}}$ , and  $\widehat{\mathcal{H}} = \widehat{\mathbf{A}} \circ \widehat{\mathcal{E}}$ .

We decompose the generalization error into a empirical error term and a estimation error term

$$\begin{aligned} \mathbb{E}_{\mathcal{S}} \mathbb{E}_{(x, x^+) \sim \mathbb{P}_{x, x^+}} &\left[ \|\widehat{\mathcal{G}}(\mathbf{x}) - \mathbf{F}(\mathbf{x})\|_2^2 + \|\widehat{\mathcal{D}} \circ \widehat{\mathcal{E}}(\mathbf{x}) - \mathbf{x}\|_2^2 + \|\widehat{\mathcal{H}}(\mathbf{x}) - \widehat{\mathcal{E}}(\mathbf{F}(\mathbf{x}))\|_2^2 + R(\widehat{\mathbf{A}}) \right] \\ &= \chi_1 + \chi_2, \end{aligned} \quad \blacksquare$$

where

$$\begin{aligned} \chi_1 &= 2\mathbb{E}_{\mathcal{S}} \left[ \frac{1}{N} \sum_{i=1}^N \left( \|\widehat{\mathcal{G}}(\mathbf{x}_i) - \mathbf{F}(\mathbf{x}_i)\|_2^2 + \|\widehat{\mathcal{D}} \circ \widehat{\mathcal{E}}(\mathbf{x}_i) - \mathbf{x}_i\|_2^2 + \|\widehat{\mathcal{H}}(\mathbf{x}_i) - \widehat{\mathcal{E}}(\mathbf{F}(\mathbf{x}_i))\|_2^2 \right) \right] \\ &+ R(\widehat{\mathbf{A}}), \end{aligned} \quad \blacksquare \tag{A.3}$$

$$\begin{aligned}
\chi_2 = & \mathbb{E}_{\mathcal{S}} \mathbb{E}_{(x, x^+) \sim \mathbb{P}_{X, X^+}} \|\widehat{\mathcal{G}}(\mathbf{x}) - \mathbf{F}(\mathbf{x})\|_2^2 - 2\mathbb{E}_{\mathcal{S}} \left[ \frac{1}{N} \sum_{i=1}^N \|\widehat{\mathcal{G}}(\mathbf{x}_i) - \mathbf{F}(\mathbf{x}_i)\|_2^2 \right] \\
& + \mathbb{E}_{\mathcal{S}} \mathbb{E}_{(x, x^+) \sim \mathbb{P}_{X, X^+}} \|\widehat{\mathcal{D}} \circ \widehat{\mathcal{E}}(\mathbf{x}) - \mathbf{x}\|_2^2 - 2\mathbb{E}_{\mathcal{S}} \left[ \frac{1}{N} \sum_{i=1}^N \|\widehat{\mathcal{D}} \circ \widehat{\mathcal{E}}(\mathbf{x}_i) - \mathbf{x}_i\|_2^2 \right] \\
\text{(A.4)} \quad & + \mathbb{E}_{\mathcal{S}} \mathbb{E}_{(x, x^+) \sim \mathbb{P}_{X, X^+}} \|\widehat{\mathcal{H}}(\mathbf{x}) - \widehat{\mathcal{E}}(\mathbf{x})\|_2^2 - 2\mathbb{E}_{\mathcal{S}} \left[ \frac{1}{N} \sum_{i=1}^N \|\widehat{\mathcal{H}}(\mathbf{x}_i) - \widehat{\mathcal{E}}(\mathbf{F}(\mathbf{x}_i))\|_2^2 \right].
\end{aligned}$$

Let  $\widetilde{\mathcal{E}}$ , and  $\widetilde{\mathcal{D}}$  be the networks in Lemma A.3 with accuracy  $\varepsilon_1 = \frac{\varepsilon}{1+C_\phi\rho\sqrt{n}} < 1$ .

For the first term  $2\mathbb{E}_{\mathcal{S}} \left[ \frac{1}{N} \sum_{i=1}^N \|\widehat{\mathcal{G}}(\mathbf{x}_i) - \mathbf{F}(\mathbf{x}_i)\|_2^2 \right]$  of  $\chi_1$ , we have

$$\begin{aligned}
2\mathbb{E}_{\mathcal{S}} \left[ \frac{1}{N} \sum_{i=1}^N \|\widehat{\mathcal{G}}(\mathbf{x}_i) - \mathbf{F}(\mathbf{x}_i)\|_2^2 \right] & \leq 2\mathbb{E}_{\mathcal{S}} \inf_{\mathcal{G} \in \mathcal{F}_{NN}^{\mathcal{G}}} \left[ \frac{1}{N} \sum_{i=1}^N \|\mathcal{G}(\mathbf{x}_i) - \mathbf{F}(\mathbf{x}_i)\|_2^2 \right] \\
& \leq 2 \inf_{\mathcal{G} \in \mathcal{F}_{NN}^{\mathcal{G}}} \mathbb{E}_{\mathcal{S}} \left[ \frac{1}{N} \sum_{i=1}^N \|\mathcal{G}(\mathbf{x}_i) - \mathbf{F}(\mathbf{x}_i)\|_2^2 \right] \\
& \leq 2\mathbb{E}_{(x, x^+) \sim \mathbb{P}_{X, X^+}} \left[ \|\widetilde{\mathcal{D}} \circ \mathbf{A}^* \circ \widetilde{\mathcal{E}}(\mathbf{x}) - \mathbf{F}(\mathbf{x})\|_2^2 \right] \\
& \leq 2D \sup_{\mathbf{x} \in \mathcal{M}} \|\widetilde{\mathcal{D}} \circ \mathbf{A}^* \circ \widetilde{\mathcal{E}}(\mathbf{x}) - \mathbf{F}(\mathbf{x})\|_{\infty}^2 \\
\text{(A.5)} \quad & \leq 2D\varepsilon^2.
\end{aligned}$$

Similarly, for the second term of  $\chi_1$ , let  $\varepsilon_1 = \min\{\frac{\varepsilon}{1+C_\phi\rho\sqrt{n}}, \frac{\varepsilon}{1+C_\phi\sqrt{n}}\}$ , we can obtain

$$\text{(A.6)} \quad 2\mathbb{E}_{\mathcal{S}} \left[ \frac{1}{N} \sum_{i=1}^N \|\widehat{\mathcal{D}} \circ \widehat{\mathcal{E}}(\mathbf{x}_i) - \mathbf{x}_i\|_2^2 \right] \leq 2D\varepsilon^2.$$

For the last term of  $\chi_1$ , we can also derive the upper bound

$$\begin{aligned}
& 2\mathbb{E}_{\mathcal{S}} \left[ \frac{1}{N} \sum_{i=1}^N \|\widehat{\mathcal{H}}(\mathbf{x}_i) - \widehat{\mathcal{E}}(\mathbf{F}(\mathbf{x}_i))\|_2^2 \right] \\
& \leq 2 \inf_{\mathcal{H} \in \mathcal{F}_{AE}^{\mathcal{H}}} \mathbb{E}_{(x, x^+) \sim \mathbb{P}_{X, X^+}} \left[ \|\mathcal{H}(\mathbf{x}) - \mathcal{E}(\mathbf{F}(\mathbf{x}))\|_2^2 \right].
\end{aligned}$$

We next bound the right-hand side by evaluating it at the candidate  $\widetilde{\mathcal{H}} := \widetilde{\mathbf{A}} \widetilde{\mathcal{E}}$ . For any  $\mathbf{x} \in \mathcal{M}$ , by the triangle inequality,

$$\begin{aligned}
\|\widetilde{\mathcal{H}}(\mathbf{x}) - \widetilde{\mathcal{E}}(\mathbf{F}(\mathbf{x}))\|_2 & \leq \|\mathbf{A}^* \widetilde{\mathcal{E}}(\mathbf{x}) - \mathbf{A}^* \varphi(\mathbf{x})\|_2 + \|\mathbf{A}^* \varphi(\mathbf{x}) - \widetilde{\mathcal{E}}(\mathbf{F}(\mathbf{x}))\|_2 \\
& \leq (\rho + 1)\sqrt{n}\varepsilon_1.
\end{aligned}$$

Choosing  $\varepsilon_1 = \min\{\frac{\varepsilon}{1+C_\phi\rho\sqrt{n}}, \frac{\varepsilon}{1+C_\phi\sqrt{n}}, \frac{\varepsilon}{(\rho+1)\sqrt{n}}\}$ , it follows that

$$\text{(A.7)} \quad 2\mathbb{E}_{\mathcal{S}} \left[ \frac{1}{N} \sum_{i=1}^N \|\widehat{\mathcal{H}}(\mathbf{x}_i) - \widehat{\mathcal{E}}(\mathbf{F}(\mathbf{x}_i))\|_2^2 \right] \leq 2n\varepsilon^2.$$

As for the last term, simply note that  $R(\widehat{\mathbf{A}}) = 0$  since  $\mathbf{A} \in \mathcal{F}_{Lin}^A$ . Thus, for the  $\chi_1$ , we can obtain

$$(A.8) \quad \chi_1 \leq 4D\varepsilon^2 + 2n\varepsilon^2.$$

We now bound the first contribution in  $\chi_2$ , defined as

$$T_1 := \mathbb{E}_{\mathcal{S}} \mathbb{E}_{(x, x^+) \sim \mathbb{P}_{\mathbf{X}, \mathbf{X}^+}} \left\| \widehat{\mathcal{G}}(\mathbf{x}) - \mathbf{F}(\mathbf{x}) \right\|_2^2 - 2\mathbb{E}_{\mathcal{S}} \left[ \frac{1}{N} \sum_{i=1}^N \left\| \widehat{\mathcal{G}}(\mathbf{x}_i) - \mathbf{F}(\mathbf{x}_i) \right\|_2^2 \right].$$

According to [25, Lemma 2], for any  $0 < \delta < 1$  we have

$$(A.9) \quad T_1 \leq \frac{35DB^2}{N} \log \mathcal{Q} \left( \frac{\delta}{2DB}, \mathcal{F}_{NN}^{\mathcal{G}}, \|\cdot\|_{L^\infty, \infty} \right) + 6\delta,$$

where  $\|f\|_{L^\infty, \infty} := \sup_{\mathbf{x}} \|f(\mathbf{x})\|_\infty$ .

It remains to estimate the covering number of the composite class  $\mathcal{F}_{NN}^{\mathcal{G}}$ . Specifically, for any  $\mathcal{G}_k = \mathcal{D}_k \circ \mathbf{A}_k \circ \mathcal{E}_k$ ,  $k = 1, 2$ , we have the uniform bound

$$\begin{aligned} & \|\mathcal{G}_1 - \mathcal{G}_2\|_{L^\infty, \infty} \\ &= \sup_{x \in \mathcal{M}} \|\mathcal{D}_1 \circ \mathbf{A}_1 \circ \mathcal{E}_1 - \mathcal{D}_2 \circ \mathbf{A}_2 \circ \mathcal{E}_1\|_{L^\infty, \infty} \\ &\leq \sup_{x \in \mathcal{M}} \left\| \mathcal{D}_1 \circ \mathbf{A}_1 \circ \mathcal{E}_1(x) - \mathcal{D}_2 \circ \mathbf{A}_1 \circ \mathcal{E}_1(x) \right\|_\infty \\ &\quad + \sup_{x \in \mathcal{M}} \left\| \mathcal{D}_2 \circ \mathbf{A}_1 \circ \mathcal{E}_1(x) - \mathcal{D}_2 \circ \mathbf{A}_2 \circ \mathcal{E}_2(x) \right\|_\infty \\ &\leq \|\mathcal{D}_1 - \mathcal{D}_2\|_{L^\infty, \infty} + C_\phi \sup_{x \in \mathcal{M}} \left\| \mathbf{A}_1 \circ \mathcal{E}_1(x) - \mathbf{A}_2 \circ \mathcal{E}_2(x) \right\|_2 \\ &\leq \|\mathcal{D}_1 - \mathcal{D}_2\|_{L^\infty, \infty} + C_\phi \sup_{x \in \mathcal{M}} \left( \|\mathbf{A}_1\|_2 \|\mathcal{E}_1(x) - \mathcal{E}_2(x)\|_2 + \|\mathbf{A}_1 - \mathbf{A}_2\|_2 \|\mathcal{E}_2(x)\|_2 \right) \\ &\leq \|\mathcal{D}_1 - \mathcal{D}_2\|_{L^\infty, \infty} + C_\phi \rho \sqrt{n} \|\mathcal{E}_1 - \mathcal{E}_2\|_{L^\infty, \infty} + C_\phi n^{3/2} \Lambda \|\mathbf{A}_1 - \mathbf{A}_2\|_{\infty, \infty}. \end{aligned}$$

Thus, we choose

$$\delta_{\mathcal{D}} := \frac{\delta}{3}, \quad \delta_{\mathcal{E}} := \frac{\delta}{3C_\phi \rho \sqrt{n}}, \quad \delta_A := \frac{\delta}{3C_\phi n^{3/2} \Lambda},$$

so that a  $\delta$ -cover of  $\mathcal{F}_{NN}^{\mathcal{G}}$  can be constructed by combining covers of the individual components,

$$\begin{aligned} & \mathcal{Q}(\delta, \mathcal{F}_{NN}^{\mathcal{G}}, \|\cdot\|_{L^\infty, \infty}) \\ &\leq \mathcal{Q}(\delta_{\mathcal{E}}, \mathcal{F}_{NN}^{\mathcal{E}}, \|\cdot\|_{L^\infty, \infty}) \cdot \mathcal{Q}(\delta_{\mathcal{D}}, \mathcal{F}_{NN}^{\mathcal{D}}, \|\cdot\|_{L^\infty, \infty}) \cdot \mathcal{Q}(\delta_A, \mathcal{F}_{Lin}^A, \|\cdot\|_{\infty, \infty}). \end{aligned}$$

It remains to bound the covering number of the linear class  $\mathcal{F}_{Lin}^A$  under the  $\|\cdot\|_{\infty, \infty}$  norm. Since  $\|A\|_{\infty, \infty} \leq \|A\|_2$ , we have  $\mathcal{F}_{Lin}^A \subset \{A : \|A\|_{\infty, \infty} \leq \rho\}$ . The covering number of the linear class  $\mathcal{F}_{Lin}^A$  under the  $\|\cdot\|_{\infty, \infty}$  norm follows from standard entropy estimates for finite-dimensional  $\ell_\infty$ -balls [35]. Hence, for any  $0 \leq \delta_A \leq \rho$ ,

$$(A.10) \quad \log \mathcal{Q}(\delta_A, \mathcal{F}_{Lin}^A, \|\cdot\|_{\infty, \infty}) \leq \mathcal{O}(n^2 (\log \rho + \log \delta_A^{-1})).$$

Applying Lemma A.2 to the encoder and decoder classes and (A.10) to the linear class yields

$$\begin{aligned} \log \mathcal{Q}\left(\frac{\delta}{2DB}, \mathcal{F}_{\text{NN}}^{\mathcal{G}}, \|\cdot\|_{L^\infty, \infty}\right) &\leq \mathcal{O}(L_{\mathcal{E}} K_{\mathcal{E}} (\log p_{\mathcal{E}} + \log \kappa_{\mathcal{E}} + \log \delta_{\mathcal{E}}^{-1})) \\ &\quad + \mathcal{O}(L_{\mathcal{D}} K_{\mathcal{D}} (\log p_{\mathcal{D}} + \log \kappa_{\mathcal{D}} + \log \delta_{\mathcal{D}}^{-1})) \\ &\quad + \mathcal{O}(n^2 (\log \rho + \log \delta_A^{-1})). \end{aligned}$$

Lemma A.3 also satisfies the architecture scaling in [25, Lemma 6 and Lemma 8], we finally obtain

$$\begin{aligned} &\log \mathcal{Q}\left(\frac{\delta}{2DB}, \mathcal{F}_{\text{NN}}^{\mathcal{G}}, \|\cdot\|_{L^\infty, \infty}\right) \\ &\leq \mathcal{O}\left(D \log^2 D \varepsilon^{-n} \log^4 \varepsilon^{-1} + D \log^2 D \varepsilon^{-n} \log^3 \varepsilon^{-1} \log \delta^{-1} + n^2 (\log \rho + \log \delta^{-1})\right). \end{aligned}$$

Setting  $\delta = \varepsilon = N^{-\frac{1}{n+2}}$ , we obtain

$$(A.11) \quad T_1 \leq \mathcal{O}\left(D^2 (\log^2 D) N^{-\frac{2}{n+2}} \log^4 N\right).$$

We next bound the remaining two contributions in  $\chi_2$ . Define

$$T_2 := \mathbb{E}_{\mathcal{S}} \mathbb{E}_{(x, x^+) \sim \mathbb{P}_{x, x^+}} \left\| \widehat{\mathcal{G}} \circ \widehat{\mathcal{E}}(\mathbf{x}) - \mathbf{x} \right\|_2^2 - 2 \mathbb{E}_{\mathcal{S}} \left[ \frac{1}{N} \sum_{i=1}^N \left\| \widehat{\mathcal{G}} \circ \widehat{\mathcal{E}}(\mathbf{x}_i) - \mathbf{x}_i \right\|_2^2 \right],$$

and

$$T_3 := \mathbb{E}_{\mathcal{S}} \mathbb{E}_{(x, x^+) \sim \mathbb{P}_{x, x^+}} \left\| \widehat{\mathcal{H}}(\mathbf{x}) - \widehat{\mathcal{E}}(\mathbf{x}) \right\|_2^2 - 2 \mathbb{E}_{\mathcal{S}} \left[ \frac{1}{N} \sum_{i=1}^N \left\| \widehat{\mathcal{H}}(\mathbf{x}_i) - \widehat{\mathcal{E}}(\mathbf{x}_i) \right\|_2^2 \right].$$

Similarly, we obtain that for any  $0 < \delta < 1$ ,

$$(A.12) \quad T_2 \leq \frac{35DB^2}{N} \log \mathcal{Q}\left(\frac{\delta}{2DB}, \mathcal{F}_{\text{NN}}^{\mathcal{G}\mathcal{E}}, \|\cdot\|_{L^\infty, \infty}\right) + 6\delta \leq \mathcal{O}\left(D^2 (\log^2 D) N^{-\frac{2}{n+2}} \log^4 N\right),$$

$$(A.13) \quad T_3 \leq \frac{35n\Lambda^2}{N} \log \mathcal{Q}\left(\frac{\delta}{2n\Lambda}, \mathcal{F}_{\text{AE}}^{\mathcal{H}}, \|\cdot\|_{L^\infty, \infty}\right) + 6\delta \leq \mathcal{O}\left(nD (\log^2 D) N^{-\frac{2}{n+2}} \log^4 N\right).$$

Combining (A.11)–(A.13) with the above covering-number bounds, we conclude that

$$\chi_2 = T_1 + T_2 + T_3 \leq \mathcal{O}\left(D^2 (\log^2 D) N^{-\frac{2}{n+2}} \log^4 N\right).$$

Consequently,

$$\begin{aligned} &\mathbb{E}_{\mathcal{S}} \mathbb{E}_{(x, x^+) \sim \mathbb{P}_{x, x^+}} \left[ \left\| \widehat{\mathcal{G}}(\mathbf{x}) - \mathbf{F}(\mathbf{x}) \right\|_2^2 + \left\| \widehat{\mathcal{G}} \circ \widehat{\mathcal{E}}(\mathbf{x}) - \mathbf{x} \right\|_2^2 + \left\| \widehat{\mathcal{H}}(\mathbf{x}) - \widehat{\mathcal{E}}(\mathbf{x}) \right\|_2^2 \right] \\ &\leq 4DN^{-\frac{2}{n+2}} + 2nN^{-\frac{2}{n+2}} + C_2 D^2 (\log^2 D) N^{-\frac{2}{n+2}} \log^4 N \\ (A.14) &\leq C D^2 (\log^2 D) N^{-\frac{2}{n+2}} \log^4 N, \end{aligned} \quad \square$$

for some constant  $C$  depending on  $n, C_\varphi, C_\phi, \Lambda, B, \rho$ , and the volume of  $\mathcal{M}$ , which completes the proof.

**References.**

- [1] Saeed Akbari, Pedram H. Dabaghian, and Omer San. Blending machine learning and sequential data assimilation over latent spaces for surrogate modeling of Boussinesq systems. *Physica D: Nonlinear Phenomena*, 448:133711, 2023.
- [2] Maddalena Amendola, Rossella Arcucci, Laetitia Mottet, César Quilodrán Casas, Shiwei Fan, Christopher Pain, Paul Linden, and Yi-Ke Guo. Data assimilation in the latent space of a convolutional autoencoder. In *Computational Science*, pages 373–386. Springer, 2021.
- [3] Ienkaran Arasaratnam and Simon Haykin. Cubature Kalman filters. *IEEE Transactions on automatic control*, 54(6):1254–1269, 2009.
- [4] Rossella Arcucci, Jiangcheng Zhu, Shuang Hu, and Yi-Ke Guo. Deep data assimilation: Integrating deep learning with data assimilation. *Applied Sciences*, 11(3):1114, 2021.
- [5] Omri Azencot, N. Benjamin Erichson, Vanessa Lin, and Michael Mahoney. Forecasting sequential data using consistent Koopman autoencoders. In *Proceedings of the 37th International Conference on Machine Learning*, volume 119 of *Proceedings of Machine Learning Research*, pages 475–485, 2020.
- [6] Marc Bocquet, Alban Farchi, and Quentin Malartic. Online learning of both state and dynamics using ensemble Kalman filters. *Foundations of Data Science*, 3(3):305–330, 2021.
- [7] Julien Brajard, Alberto Carrassi, Marc Bocquet, and Laurent Bertino. Combining data assimilation and machine learning to emulate a dynamical model from sparse and noisy observations: A case study with the Lorenz 96 model. *Journal of Computational Science*, 44:101171, 2020.
- [8] Steven L. Brunton, Marko Budišić, Eurika Kaiser, and J. Nathan Kutz. Modern Koopman theory for dynamical systems. *SIAM Review*, 64(2):229–340, 2022.
- [9] Mark Buehner, P. L. Houtekamer, Cecilien Charette, Herschel L. Mitchell, and Bin He. Intercomparison of variational data assimilation and the ensemble Kalman filter for global deterministic NWP. Part I: Description and single-observation experiments. *Monthly Weather Review*, 138(5):1550–1566, 2010.
- [10] Caterina Buizza, César Quilodrán Casas, Philip Nadler, Julian Mack, Stefano Marrone, Zainab Titus, Clémence Le Cornec, Evelyn Heylen, Tolga Dur, Luis Baca Ruiz, Claire Heaney, Julio Amador Díaz Lopez, K.S. Sesh Kumar, and Rossella Arcucci. Data learning: Integrating data assimilation and machine learning. *Journal of Computational Science*, 58:101525, 2022.
- [11] Ethan Che, Jing Dong, and Xin T Tong. Stochastic gradient descent with adaptive data. *arXiv:2410.01195*, 2024.
- [12] Minshuo Chen, Haoming Jiang, Wenjing Liao, and Tuo Zhao. Nonparametric regression on low-dimensional manifolds using deep ReLU networks: function approximation and statistical recovery. *Information and Inference: A Journal of the IMA*, 11(4):1203–1253, 2022.
- [13] Sibó Cheng, Jianhua Chen, Charitos Anastasiou, Panagiota Angeli, Omar K Matar, Yi-Ke Guo, Christopher C Pain, and Rossella Arcucci. Generalised latent assimilation in heterogeneous reduced spaces with machine learning surrogate models. *Journal of Scientific Computing*, 94(1):11, 2023.
- [14] Sibó Cheng, I. Colin Prentice, Yuhan Huang, Yufang Jin, Yi-Ke Guo, and Rossella Arcucci. Data-driven surrogate model with latent data assimilation: Application to wildfire forecasting. *Journal of Computational Physics*, 464:111302, 2022.
- [15] Sibó Cheng, Yilin Zhuang, Lyes Kahouadji, Che Liu, Jianhua Chen, Omar K. Matar, and Rossella Arcucci. Multi-domain encoder–decoder neural networks

- for latent data assimilation in dynamical systems. *Computer Methods in Applied Mechanics and Engineering*, 430:117201, 2024.
- [16] Alexander Cloninger and Timo Klock. A deep network construction that adapts to intrinsic dimensionality beyond the domain. *Neural Networks*, 141:404–419, 2021.
- [17] Geir Evensen. *Data assimilation: the ensemble Kalman filter*. Springer, 2009.
- [18] Simon J Julier and Jeffrey K Uhlmann. New extension of the Kalman filter to nonlinear systems. In *Signal processing, sensor fusion, and target recognition VI*, volume 3068, pages 182–193, 1997.
- [19] Eugenia Kalnay. *Atmospheric Modeling, Data Assimilation and Predictability*. Cambridge University Press, 2002.
- [20] David Kelly, Andrew J Majda, and Xin T Tong. Concrete ensemble kalman filters with rigorous catastrophic filter divergence. *Proceedings of the National Academy of Sciences*, 112(34):10589–10594, 2015.
- [21] Yuehaw Khoo, Xin T Tong, Wanjie Wang, and Yuguan Wang. Temporal label recovery from noisy dynamical data. *arXiv:2406.13635*, 2024.
- [22] Mojzesz Kirszbraun. Über die zusammenziehende und Lipschitzsche Transformationen. *Fundamenta Mathematicae*, 22:77–108, 1934.
- [23] John M Lee. *Riemannian manifolds: an introduction to curvature*, volume 176. Springer Science & Business Media, 2006.
- [24] Zhuoyuan Li, Bin Dong, and Pingwen Zhang. Latent assimilation with implicit neural representations for unknown dynamics. *Journal of Computational Physics*, 506:112953, 2024.
- [25] Hao Liu, Alex Havrilla, Rongjie Lai, and Wenjing Liao. Deep nonparametric estimation of intrinsic data structures by chart autoencoders: Generalization error and robustness. *Applied and Computational Harmonic Analysis*, 68:101602, 2024.
- [26] Ningxin Liu, Shuigen Liu, Xin T Tong, and Lijian Jiang. Estimate of Koopman modes and eigenvalues with Kalman filter. *arXiv: 2410.02815*, 2024.
- [27] Shuigen Liu, Sebastian Reich, and Xin T Tong. Dropout ensemble kalman inversion for high dimensional inverse problems. *SIAM Journal on Numerical Analysis*, 63(2):685–715, 2025.
- [28] Indranil Nayak, Ananda Chakrabarti, Mrinal Kumar, Fernando L Teixeira, and Debdipta Goswami. Temporally-consistent koopman autoencoders for forecasting dynamical systems. *Scientific Reports*, 15(1):22127, 2025.
- [29] Mathis Peyron, Anthony Fillion, Selime Gürol, Victor Marchais, Serge Gratton, Pierre Boudier, and Gael Goret. Latent space data assimilation by using deep learning. *Quarterly Journal of the Royal Meteorological Society*, 147(740):3759–3777, 2021.
- [30] Sebastian Reich and Colin Cotter. *Probabilistic forecasting and Bayesian data assimilation*. Cambridge University Press, 2015.
- [31] Alessio Spantini, Ricardo Baptista, and Youssef Marzouk. Coupling techniques for nonlinear ensemble filtering. *SIAM Review*, 64(4):921–953, 2022.
- [32] Floris Takens. Detecting strange attractors in turbulence. In *Dynamical Systems and Turbulence, Warwick 1980*, pages 366–381, Berlin, Heidelberg, 1981. Springer Berlin Heidelberg.
- [33] Joshua B. Tenenbaum, Vin de Silva, and John C. Langford. A global geometric framework for nonlinear dimensionality reduction. *Science*, 290(5500):2319–2323, 2000.
- [34] Xin T Tong, Andrew J Majda, and David Kelly. Nonlinear stability of the ensemble Kalman filter with adaptive covariance inflation. *Communications in*

- Mathematical Sciences*, 14:1283–1313, 2016.
- [35] A. W. van der Vaart and Jon A. Wellner. *Weak convergence and empirical processes: with applications to statistics*. Mathematics and Statistics, 1996.
  - [36] Yanyan Wang and Liang Yan. Data-driven operator inference for parameter estimation in nonlinear partial differential equations. *Journal of Computational Physics*, 544:114442, 2026.
  - [37] Yanyan Wang, Liang Yan, and Tao Zhou. Deep learning-enhanced reduced-order ensemble Kalman filter for efficient Bayesian data assimilation of parametric PDEs. *Computer Physics Communications*, 311:109544, 2025.
  - [38] Dmitry Yarotsky. Error bounds for approximations with deep ReLU networks. *Neural Networks*, 94:103–114, 2017.
  - [39] Jiangcheng Zhu, Shuang Hu, Rossella Arcucci, Chao Xu, Jihong Zhu, and Yi-ke Guo. Model error correction in data assimilation by integrating neural networks. *Big Data Mining and Analytics*, 2(2):83–91, 2019.